

Entropic Optimal Transport Eigenmaps for Nonlinear Alignment and Joint Embedding of High-Dimensional Datasets

Boris Landa^{1,2,*} Yuval Kluger^{2,4,5} Rong Ma^{3,†}

¹Department of Electrical Engineering, Yale University

²Program in Applied Mathematics, Yale University

³Department of Biostatistics, Harvard University

⁴Interdepartmental Program in Computational Biology and Bioinformatics, Yale University

⁵Department of Pathology, Yale University School of Medicine

*Corresponding author. Email: boris.landa@yale.edu

†Corresponding author. Email: rongma@hsph.harvard.edu

July 3, 2024

Abstract

Embedding high-dimensional data into a low-dimensional space is an indispensable component of data analysis. In numerous applications, it is necessary to align and jointly embed multiple datasets from different studies or experimental conditions. Such datasets may share underlying structures of interest but exhibit individual distortions, resulting in misaligned embeddings using traditional techniques. In this work, we propose *Entropic Optimal Transport (EOT) eigenmaps*, a principled approach for aligning and jointly embedding a pair of datasets with theoretical guarantees. Our approach leverages the leading singular vectors of the EOT plan matrix between two datasets to extract their shared underlying structure and align the datasets accordingly in a common embedding space. We interpret our approach as an inter-data variant of the classical Laplacian eigenmaps and diffusion maps embeddings, showing that it enjoys many favorable analogous properties. We then analyze a data-generative model where two observed high-dimensional datasets share latent variables on a common low-dimensional manifold, but each dataset is subject to data-specific translation, scaling, nuisance structures, and noise. We show that in a high-dimensional asymptotic regime, the EOT plan recovers the shared manifold structure by approximating a kernel function evaluated at the locations of the latent variables. Subsequently, we provide a geometric interpretation of our embedding by relating it to the eigenfunctions of population-level operators encoding the density and geometry of the shared manifold. Finally, we showcase the performance of our approach for data integration and embedding through simulations and analyses of real-world biological data, demonstrating its advantages over alternative methods in challenging scenarios.

Keywords— data integration, low-dimensional embedding, dimensionality reduction, manifold learning, batch effects, graph Laplacian, Laplacian eigenmaps, diffusion maps, entropic optimal transport

1 Introduction

The challenge of effectively analyzing high-dimensional data is prevalent across many scientific disciplines. Techniques for embedding high-dimensional data into lower-dimensional spaces are commonly utilized to simplify complex data and aid in various data analytic tasks including clustering, visualization, and manifold learning. Traditional embedding and dimensionality reduction methods primarily focus on extracting low-dimensional structures from a single dataset. Specifically, given a dataset $\mathcal{X} = \{x_1, \dots, x_m\} \subset \mathbb{R}^p$, their

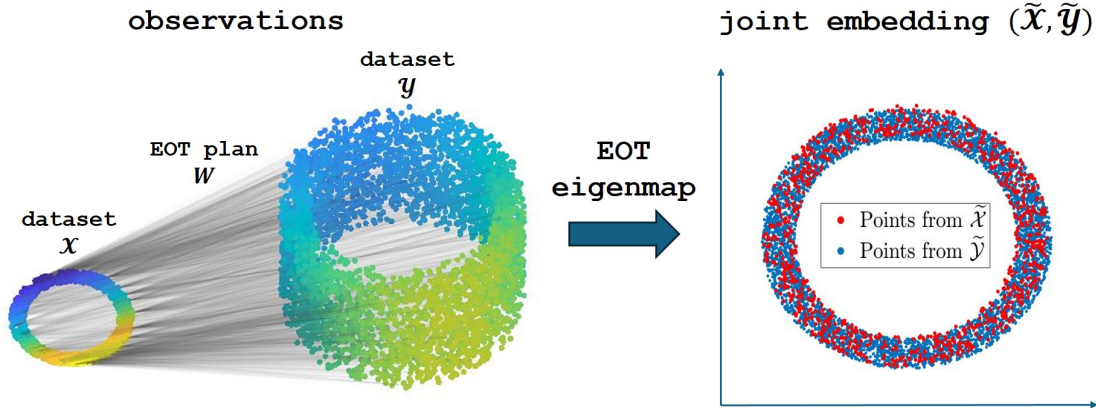


Figure 1: Datasets \mathcal{X} and \mathcal{Y} in \mathbb{R}^3 (left) and their joint embedding $(\tilde{\mathcal{X}}, \tilde{\mathcal{Y}})$ in \mathbb{R}^2 (right) using EOT eigenmaps. The dataset \mathcal{X} contains $m = 1,000$ samples from an annulus in the XY-plane, while \mathcal{Y} contains $n = 5,000$ samples from a shifted and scaled version of the same annulus with additional variation along the Z-axis. The transport plan $W \in \mathbb{R}^{m \times n}$ encodes the cross-data pairwise affinities between the points of \mathcal{X} and \mathcal{Y} . Our proposed method embeds \mathcal{X} (\mathcal{Y}) into \mathbb{R}^2 using the second and third left (right) singular vectors of W , up to a suitable scaling (see eq. (5) in Section 2.1 with $q = 2$ and $t = 0$). On the left, the points of \mathcal{X} (\mathcal{Y}) are colored according to the second left (right) singular vector of W , highlighting the correspondence between the datasets. Our joint embedding captures the underlying structure shared between the datasets in the XY-plane and aligns the datasets accordingly.

goal is to embed \mathcal{X} into \mathbb{R}^q , producing $\tilde{\mathcal{X}} = \{\tilde{x}_1, \dots, \tilde{x}_m\} \subset \mathbb{R}^q$, typically with $q \ll p$. To capture nonlinear structures in the data, popular techniques such as Laplacian eigenmaps [7], diffusion maps [15], t-distributed Stochastic Neighbor Embedding (tSNE) [44], and UMAP [6], first construct a similarity graph over the data points in \mathbb{R}^p , represented by an affinity matrix $W \in \mathbb{R}^{m \times m}$. Then, the embedded data points are arranged in \mathbb{R}^q according to W , preserving key structural characteristics of the data.

In many modern applications such as genomics [62], precision medicine [55] and business analytics [17], there is a need to integrate and jointly analyze multiple datasets. Specifically, in single-cell omics research, to understand a biological process of interest, it is common that multiple high-dimensional datasets are generated using the same type of omics assays but based on different samples or experimental conditions [61, 5, 39]. Such datasets may share common low-dimensional structures that characterize the underlying biological process. However, due to variations in biological samples or experimental conditions, each dataset may exhibit unique deformations, corruptions, and nuisance structures. These phenomena are commonly known as batch effects in genomics and related fields [23, 62]. To effectively analyze such datasets, it is desirable to embed them jointly into a lower-dimensional space while preserving their common underlying structures and filtering out individual distortions.

Here, we consider a setup with two datasets, $\mathcal{X} = \{x_1, \dots, x_m\} \subset \mathbb{R}^p$ and $\mathcal{Y} = \{y_1, \dots, y_n\} \subset \mathbb{R}^p$, where the goal is to jointly embed them into \mathbb{R}^q as $\tilde{\mathcal{X}} = \{\tilde{x}_1, \dots, \tilde{x}_m\} \subset \mathbb{R}^q$ and $\tilde{\mathcal{Y}} = \{\tilde{y}_1, \dots, \tilde{y}_n\} \subset \mathbb{R}^q$, respectively. A naive approach is to concatenate the datasets, i.e., to form $\{\mathcal{X}, \mathcal{Y}\}$, and then apply standard off-the-shelf embedding techniques. However, if dataset-specific distortions are present, traditional methods [51, 56, 60, 19] typically fail to extract or preserve common structures in the concatenated data, resulting in embeddings where $\tilde{\mathcal{X}}$ and $\tilde{\mathcal{Y}}$ are misaligned [41, 43]; see also Figure 2 in Section 4 for numerical evidence. To address this issue, numerous approaches adopt a multi-step process in which the datasets are explicitly aligned, e.g., using affine transformations, either before or after the embedding [60, 26, 4, 37]. Other common approaches rely on nonlinear functions such as neural networks to generate embeddings where the datasets are optimally aligned according to a prescribed loss function [54, 35, 38, 11, 18]. However, most existing techniques were designed for specialized applications and are difficult to interpret in more general settings [13, 41, 3]. Moreover, their analytical properties are often not well understood, especially under challenging conditions involving data-specific distortions or imbalances in signal magnitude and sample size.

In this work, we propose a principled approach for aligning a pair of high-dimensional datasets \mathcal{X} and \mathcal{Y} and embedding them jointly into \mathbb{R}^q . Our approach, termed *Entropic Optimal Transport eigenmaps*, is naturally interpretable and is amenable to theoretical analysis under challenging conditions frequently

encountered in real-world applications. Our technique relies on Entropic Optimal Transport (EOT) between distributions [16, 50] – a regularized variant of classical Optimal Transport (OT) [66]. EOT is a popular approach for approximating OT due to its numerous computational and statistical benefits; see, e.g., [47, 49, 12, 36] and references therein. Here, we utilize the EOT transport plan between the datasets \mathcal{X} and \mathcal{Y} under the Euclidean distance. This transport plan encodes the inter-data pairwise affinities between points in \mathcal{X} and \mathcal{Y} , represented by a nonnegative matrix $W \in \mathbb{R}^{m \times n}$. We then use the leading nontrivial singular vectors of W after a suitable rescaling to embed \mathcal{X} and \mathcal{Y} into \mathbb{R}^q ; see Section 2.1 for a description of EOT and our method in Algorithm 1. Figure 1 illustrates our setup and proposed approach.

Our main contributions are as follows. Firstly, we justify our method by presenting several useful interpretations of the proposed embedding in finite samples. In particular, we establish connections to the classical Laplacian eigenmaps and diffusion maps embeddings, showing that our approach enjoys many favorable properties analogous to these methods; see Sections 2.2 and 2.3. Secondly, in Section 3, we analyze a data-generative model in which the datasets share a common low-dimensional manifold structure governed by latent variables of interest, whereas each dataset exhibits distinct translation, scaling, nuisance variables, and sub-Gaussian noise. The noise can be strong, dependent, and heteroskedastic in each dataset. We establish that for high dimension p and large sample sizes m and n , the EOT plan W approximates a doubly stochastic Gaussian kernel evaluated at the locations of the latent variables on the shared manifold. The bandwidth of this kernel depends on the scaling of the datasets but is otherwise invariant to the deformations and corruptions. We then relate our embedding to the eigenfunctions of a suitable integral operator on the manifold. In particular, for small EOT regularization parameters, this operator is closely related to the so-called symmetric normalized graph Laplacian commonly used for spectral clustering and manifold learning. Overall, our analysis highlights the robustness of our approach to dataset-specific deformations and corruptions and its capability to reliably extract and embed low-dimensional structures shared by two datasets, akin to traditional Laplacian-based techniques on single datasets. Finally, in Sections 4 and 5, we demonstrate the practical advantages of our approach on simulated and real biological data. In particular, we show that our method achieves better and more reliable alignment of single-cell omics datasets such as single-cell RNA-sequencing (scRNA-seq) and single-cell ATAC-sequencing (scATAC-seq) than alternative methods. Applying our method to single-cell multi-omic datasets where different types of features are measured for the same cells, we demonstrate the usefulness of the proposed method in multi-view analysis, inferring interactions between epigenome and transcriptome. The R codes of our proposed methods and those used to generate our numerical results are accessible at our GitHub repository <https://github.com/rongstat/EOT-eigenmap>.

2 Method, properties, and interpretations

2.1 EOT and the proposed embedding

Let $\mathcal{X} = \{x_1, \dots, x_m\} \subset \mathbb{R}^p$ and $\mathcal{Y} = \{y_1, \dots, y_n\} \subset \mathbb{R}^p$ be two given datasets, assuming without loss of generality that $m \leq n$ (otherwise, we can always interchange the roles of \mathcal{X} and \mathcal{Y}). We denote the affinity between x_i and y_j as $W_{i,j}$, where $W \in \mathbb{R}^{m \times n}$ is the entropic optimal transport (EOT) plan between \mathcal{X} and \mathcal{Y} using the Euclidean distance [50]. Specifically,

$$W = \operatorname{argmin}_{W' \in \mathcal{B}_{m,n}} \left\{ \sum_{i,j} \|x_i - y_j\|_2^2 W'_{i,j} + \varepsilon \sum_{i,j} W'_{i,j} \log W'_{i,j} \right\}, \quad (1)$$

where $\varepsilon \geq 0$ is the entropic regularization parameter and $\mathcal{B}_{m,n}$ is the set of feasible transport plans,

$$\mathcal{B}_{m,n} = \left\{ A \in \mathbb{R}^{m \times n} : A_{i,j} \geq 0, \sum_{k=1}^n A_{i,k} = \sqrt{\frac{n}{m}}, \sum_{\ell=1}^m A_{\ell,j} = \sqrt{\frac{m}{n}}, i = 1, \dots, m, j = 1, \dots, n \right\}. \quad (2)$$

We remark that the above definition of $\mathcal{B}_{m,n}$ uses a specific scaling of the transport plan that is more convenient for our purposes, where the entries of A sum to \sqrt{mn} rather than 1 as in other existing works.

When $\varepsilon = 0$, the matrix W describes the exact optimal plan to redistribute mass from a uniform distribution on \mathcal{X} to a uniform distribution on \mathcal{Y} or vice versa, minimizing the total transport cost between

Algorithm 1 EOT eigenmaps

Input: Data matrices $\mathcal{X} = \{x_1, \dots, x_m\} \subset \mathbb{R}^p$ and $\mathcal{Y} = \{y_1, \dots, y_n\} \subset \mathbb{R}^p$ with $m \leq n$, embedding dimension $q \leq m - 1$, EOT regularization parameter $\varepsilon > 0$, and $t \geq 0$.

- 1: Compute the EOT plan $W \in \mathbb{R}^{m \times n}$ defined in (1), e.g., by scaling the rows and columns of the Gaussian kernel matrix K from (3) using the Sinkhorn-Knopp algorithm [59] such that each row sums to $\sqrt{n/m}$ and each column sums to $\sqrt{m/n}$.
 - 2: Compute the leading q nontrivial left singular vectors, right singular vectors, and singular values of W , denoted by $\{\mathbf{u}_2, \dots, \mathbf{u}_{q+1}\}$, $\{\mathbf{v}_2, \dots, \mathbf{v}_{q+1}\}$, and $\{s_2, \dots, s_{q+1}\}$, respectively.
 - 3: Form the embedded datasets $\tilde{\mathcal{X}} = \{\tilde{x}_1, \dots, \tilde{x}_m\} \subset \mathbb{R}^q$ and $\tilde{\mathcal{Y}} = \{\tilde{y}_1, \dots, \tilde{y}_n\} \subset \mathbb{R}^q$ according to (5).
-

the source and target points as measured by the squared Euclidean distance. In this context, $W_{i,j}/\sqrt{mn}$ is the relative mass transported from x_i to y_j (or vice versa). The resulting transport plan is generally sparse and may not be unique. When $\varepsilon > 0$, the entropic regularization term $\varepsilon \sum_{i,j} W'_{i,j} \log W'_{i,j}$ penalizes sparsity in the transport plan and forces the redistribution of mass to be less concentrated and more spread out. In this case, the regularized transport cost minimized in (1) is strictly convex, and the transport plan W is uniquely defined. Moreover, the solution can be expressed explicitly by diagonally scaling the rows and columns of a cross-dataset Gaussian kernel matrix with bandwidth parameter ε [16, 50]. Specifically,

$$W_{i,j} = \alpha_i K_{i,j} \beta_j, \quad K_{i,j} = \exp \left\{ -\frac{\|x_i - y_j\|^2}{\varepsilon} \right\}, \quad (3)$$

where $\alpha = [\alpha_1, \dots, \alpha_m]$ and $\beta = [\beta_1, \dots, \beta_n]$ are chosen such that $W \in \mathcal{B}_{m,n}$, i.e., such that each row of W sums to $\sqrt{n/m}$ and each column of W sums to $\sqrt{m/n}$. The vectors α and β always exist and are unique up to a trivial scalar ambiguity. Moreover, they can be computed efficiently by the classical Sinkhorn-Knopp algorithm [57, 59]; see also [1] and references therein for more recent algorithmic developments. From this point onward, we will assume that $\varepsilon > 0$.

We denote the (compact) singular value decomposition (SVD) of W as

$$W = USV^T, \quad U = [\mathbf{u}_1, \dots, \mathbf{u}_m], \quad V = [\mathbf{v}_1, \dots, \mathbf{v}_m], \quad S = \text{diag}\{s_1, \dots, s_m\}, \quad (4)$$

where $\{\mathbf{u}_i\}_{i=1}^m \in \mathbb{R}^m$, $\{\mathbf{v}_i\}_{i=1}^m \in \mathbb{R}^n$, and $\{s_i\}_{i=1}^m$ are the left singular vectors, right singular vectors, and singular values (sorted in descending order) of W , respectively. Since W is entrywise positive and in $\mathcal{B}_{m,n}$, the first pair of singular vectors of W is trivial [28]: $\mathbf{u}_1 = \mathbf{1}_m/\sqrt{m}$, $\mathbf{v}_1 = \mathbf{1}_n/\sqrt{n}$, and $1 = s_1 > s_2$, where $\mathbf{1}_m$ ($\mathbf{1}_n$) is a vector of m (n) ones.

We propose to embed \mathcal{X} and \mathcal{Y} into \mathbb{R}^q using the leading q nontrivial left and right singular vectors of W , respectively, up to a suitable scaling. Specifically, given a desired embedding dimension $q \leq m - 1$ and a parameter $t \geq 0$, the embedded datasets $\tilde{\mathcal{X}} = \{\tilde{x}_1, \dots, \tilde{x}_m\} \subset \mathbb{R}^q$ and $\tilde{\mathcal{Y}} = \{\tilde{y}_1, \dots, \tilde{y}_n\} \subset \mathbb{R}^q$ are defined by

$$\tilde{x}_i = \sqrt{m} \begin{bmatrix} s_2^t \mathbf{u}_2[i] \\ \vdots \\ s_{q+1}^t \mathbf{u}_{q+1}[i] \end{bmatrix}, \quad \tilde{y}_j = \sqrt{n} \begin{bmatrix} s_2^t \mathbf{v}_2[j] \\ \vdots \\ s_{q+1}^t \mathbf{v}_{q+1}[j] \end{bmatrix}, \quad (5)$$

for $i = 1, \dots, m$ and $j = 1, \dots, n$, where $u_k[i]$ ($v_k[j]$) denotes the i 'th (j 'th) coordinate of u_k (v_k). The parameter t here controls the scaling of the embedding coordinates; all coordinates are equally weighted for $t = 0$ while for $t > 0$, coordinates that correspond to smaller singular values of W exhibit more rapid decay as t increases. Our proposed method, termed *EOT eigenmaps*, is summarized in Algorithm 1. Below we derive important properties of our approach and present its interpretation in two special cases: $t = 0$ and integers $t > 0$. This allows us to gain insights and establish connections to existing techniques, particularly Laplacian eigenmaps and diffusion maps, which have been extensively studied for embedding a single dataset. Additional discussions regarding the hyperparameters (ε, q, t) can be found in Appendix H.

2.2 The case of $t = 0$: inter-data Laplacian eigenmaps

For the case of $t = 0$, we interpret our approach as an inter-data variant of Laplacian eigenmaps [7]. In Laplacian eigenmaps, the points of a single dataset are mapped to the embedding space according to the pairwise affinities between the points in the ambient space. Specifically, the embedded data points are obtained from the leading eigenvectors of the graph Laplacian constructed from the affinity matrix. In what follows, we show that our proposed embedding solves an optimal data alignment problem closely related to the one solved by Laplacian eigenmaps for a single dataset. We then establish that our embedding can be obtained from the eigenvectors of a certain *inter-data graph Laplacian*. We characterize the properties of this graph Laplacian to obtain useful interpretations and insights on our approach.

Our first result states that our proposed method aligns two datasets optimally in the embedding space according to the pairwise affinities measured by the EOT plan in the ambient space. In particular, we show that the low-dimensional embedded datasets $\tilde{\mathcal{X}}$ and $\tilde{\mathcal{Y}}$ achieve the minimal transport cost in \mathbb{R}^q under the transport plan W from (3) and the constraints that the coordinates of each embedded dataset have zero means, unit variances, and are pairwise uncorrelated (orthogonal). Concretely, consider the objective function

$$J(\mathcal{X}', \mathcal{Y}') = \sum_{ij} \|x'_i - y'_j\|_2^2 W_{i,j}, \quad (6)$$

for $\mathcal{X}' = \{x'_1, \dots, x'_m\} \subset \mathbb{R}^q$ and $\mathcal{Y}' = \{y'_1, \dots, y'_n\} \subset \mathbb{R}^q$, with $q \leq m - 1$, and the constraints

$$\frac{1}{m} \sum_{i=1}^m x'_i[k] = 0, \quad \frac{1}{n} \sum_{j=1}^n y'_j[k] = 0, \quad \frac{1}{m} \sum_{i=1}^m x'_i[k] x'_i[\ell] = \delta_{k,\ell}, \quad \frac{1}{n} \sum_{j=1}^n y'_j[k] y'_j[\ell] = \delta_{k,\ell}, \quad (7)$$

for all $k, \ell = 1, \dots, q$, where $\delta_{k,\ell}$ is the Kronecker delta ($\delta_{k,\ell} = 1$ if $k = \ell$ and $\delta_{k,\ell} = 0$ otherwise). Note that the objective function in (6) has the same form as the one being minimized in (1) to obtain the EOT plan albeit the entropic regularization term – this term does not influence the minimization over \mathcal{X}' and \mathcal{Y}' since in (6) W is given. In particular, if the two datasets are identical, i.e., $\mathcal{X} = \mathcal{Y}$, then the cost function (6) is the same as the one minimized in Laplacian eigenmaps [7], except that the doubly stochastic affinity matrix W [71, 45, 34] here replaces the traditional (un-normalized) Gaussian kernel matrix used in Laplacian eigenmaps. The following proposition, whose proof can be found in Appendix A, establishes the optimality of (5) with $t = 0$ for aligning the embedded datasets with respect to W .

Proposition 1. *Under the constraints (7), the function $J(\mathcal{X}', \mathcal{Y}')$ from (6) is minimized by $(\tilde{\mathcal{X}}, \tilde{\mathcal{Y}})$ from (5) with $t = 0$.*

By Proposition 1, the coordinates of the points minimizing the transport cost (6) under the constraints (7) are given by the leading q nontrivial singular vectors of W after rescaling the left singular vectors by \sqrt{m} and the right singular vectors by \sqrt{n} . We note that this minimizer is not unique and may be subject to rotation and reflection. For instance, replacing $(\mathbf{u}_k, \mathbf{v}_k)$ by $(-\mathbf{u}_k, -\mathbf{v}_k)$ will leave the transport cost unchanged.

Next, we establish a connection between our embedding for $t = 0$ and a certain graph Laplacian-type matrix and its eigen-decomposition. Define the matrices $\hat{W}, L, D, \tilde{L} \in \mathbb{R}^{(m+n) \times (m+n)}$ according to

$$\hat{W} = \begin{bmatrix} \mathbf{0}_{m \times m} & W \\ W^T & \mathbf{0}_{n \times n} \end{bmatrix}, \quad L = I_{m+n} - \hat{W}, \quad D = \begin{bmatrix} \sqrt{m} I_m & \mathbf{0}_{m \times n} \\ \mathbf{0}_{n \times m} & \sqrt{n} I_n \end{bmatrix}, \quad \tilde{L} = D L D^{-1}, \quad (8)$$

where I_n is the $n \times n$ identity matrix. The matrix \hat{W} is the adjacency matrix of an undirected bipartite graph \mathcal{G} whose nodes are the points of \mathcal{X} and \mathcal{Y} and the edge weights are given by the EOT plan W . Let $\mathbf{f} \in \mathbb{R}^{m+n}$ be a column vector describing a function over the (nodes of the) graph \mathcal{G} and denote $\mathbf{f} = [\mathbf{g}^T, \mathbf{h}^T]^T$, where $\mathbf{g} \in \mathbb{R}^m$ and $\mathbf{h} \in \mathbb{R}^n$ are column vectors interpreted as functions over the graph nodes corresponding to \mathcal{X} and \mathcal{Y} , respectively. The following proposition, whose proof can be found in Appendix B, provides several useful properties of L and \tilde{L} .

Proposition 2. *The following holds:*

1. L is symmetric and positive semidefinite (PSD) with eigenvalues (sorted in ascending order) $\{\lambda_1, \dots, \lambda_{m+n}\} = \{0, 1 - s_2, \dots, 1 - s_m, 1, \dots, 1, 1 + s_m, \dots, 1 + s_2, 2\}$ and corresponding orthonormal eigenvectors $\phi_1, \dots, \phi_{m+n} \in \mathbb{R}^{m+n}$ given in Appendix B. Moreover, L admits the quadratic form

$$\mathbf{f}^T L \mathbf{f} = \frac{1}{\sqrt{mn}} \sum_{ij} (\sqrt{m}\mathbf{g}[i] - \sqrt{n}\mathbf{h}[j])^2 W_{i,j}. \quad (9)$$

2. \tilde{L} is eigen-decomposable with the same eigenvalues $\{\lambda_k\}$ of L and corresponding eigenvectors $\psi_k = D\phi_k / \|D\phi_k\|_2$ for $k = 1, \dots, m+n$. Specifically, $\psi_1 = \mathbf{1}_{m+n} / \sqrt{m+n}$, and for $k = 2, \dots, q+1 \leq m$,

$$\psi_k = \frac{1}{\sqrt{m+n}} \begin{bmatrix} \sqrt{m}\mathbf{u}_k \\ \sqrt{n}\mathbf{v}_k \end{bmatrix} = \frac{1}{\sqrt{m+n}} \begin{bmatrix} \tilde{x}_1[k-1] \\ \vdots \\ \tilde{x}_m[k-1] \\ \tilde{y}_1[k-1] \\ \vdots \\ \tilde{y}_n[k-1] \end{bmatrix}. \quad (10)$$

For a given function $\mathbf{f} = [\mathbf{g}^T, \mathbf{h}^T]^T$ on the graph \mathcal{G} , the quadratic form in (9) quantifies the similarity between \mathbf{g} and \mathbf{h} with respect to the graph edge weights W after rescaling \mathbf{g} and \mathbf{h} by \sqrt{m} and \sqrt{n} , respectively. This rescaling is natural for comparing \mathbf{g} and \mathbf{h} if $\|\mathbf{g}\|_2 = \|\mathbf{h}\|_2$, since in this case we have $\|\sqrt{m}\mathbf{g}\|_2^2/m = \|\sqrt{n}\mathbf{h}\|_2^2/n$, making the individual entries of $\sqrt{m}\mathbf{g}$ and $\sqrt{n}\mathbf{h}$ comparable with the same average magnitude, irrespective of the dataset sizes. If the sizes of the datasets are the same, i.e., $m = n$, then L becomes the standard graph Laplacian for the graph \mathcal{G} . Otherwise, L can be interpreted as an inter-data graph Laplacian for imbalanced datasets.

The functions over the graph \mathcal{G} that minimize the quadratic form (9) are given by the eigenvectors of L with the smallest eigenvalues. Specifically, the vectors ϕ_k with small indices k constitute orthonormal functions over the graph \mathcal{G} , each of the form $[\mathbf{g}^T, \mathbf{h}^T]^T$, such that $\sqrt{m}\mathbf{g}$ and $\sqrt{n}\mathbf{h}$ are similar with respect to the graph weights W . These vectors $\sqrt{m}\mathbf{g}$ and $\sqrt{n}\mathbf{h}$ are given precisely by the first m coordinates and the last n coordinates, respectively, of the eigenvectors ψ_k of \tilde{L} (since ψ_k is proportional to $D\phi_k$). Indeed, observe that

$$\frac{m+n}{\sqrt{mn}} \sum_{ij} (\psi_k[i] - \psi_k[m+j])^2 W_{i,j} = \frac{1}{\sqrt{mn}} \sum_{ij} (\sqrt{m}\mathbf{u}_k[i] - \sqrt{n}\mathbf{v}_k[j])^2 W_{i,j} = \phi_k^T L \phi_k = \lambda_k. \quad (11)$$

Therefore, for smaller eigenvalues λ_k , the two parts of ψ_k (corresponding to \mathcal{X} and \mathcal{Y}) are more similar to each other. We conclude that the leading nontrivial eigenvectors of \tilde{L} are the non-constant orthonormal functions over the bipartite graph \mathcal{G} that are the most similar across the two parts of the graph. These eigenvectors constitute the coordinates of the embedded data $\{\tilde{\mathcal{X}}, \tilde{\mathcal{Y}}\}$ from (5) for $t = 0$ up to the factor $\sqrt{m+n}$.

Finally, note that the transport cost (6) for the embedded data can be expressed as

$$J(\tilde{\mathcal{X}}, \tilde{\mathcal{Y}}) = \sum_{ij} \|\tilde{x}_i - \tilde{y}_j\|_2^2 W_{i,j} = \sum_{k=2}^{q+1} \sum_{ij} (\sqrt{m}\mathbf{u}_k[i] - \sqrt{n}\mathbf{v}_k[j])^2 W_{i,j} = 2\sqrt{mn} \sum_{k=2}^{q+1} \phi_k^T L \phi_k = 2\sqrt{mn} \sum_{k=2}^{q+1} \lambda_k. \quad (12)$$

Hence, the leading q nontrivial eigenvalues of L (or \tilde{L}) quantify the discrepancy between the embedded datasets $\tilde{\mathcal{X}}$ and $\tilde{\mathcal{Y}}$ according to the transport plan W . The smaller these eigenvalues are, the better aligned are the embedded datasets in \mathbb{R}^q . Since the magnitude of each embedding coordinate is constrained according to (7), the cost $J(\tilde{\mathcal{X}}, \tilde{\mathcal{Y}})$ always increases with the embedding dimension q .

2.3 The case of an integer $t > 0$: inter-data diffusion maps

We now consider the case of an integer $t > 0$ in the embedding (5). In this case, we interpret our approach as an inter-data variant of diffusion maps [15]. In what follows, we relate our embedding to a random walk on

the bipartite graph \mathcal{G} and establish that our embedding preserves a suitable diffusion distance derived from this random walk, where t is the number of steps taken.

We begin by defining the matrix $P \in \mathbb{R}^{(m+n) \times (m+n)}$ as

$$P = I_{m+n} - \tilde{L} = D\hat{W}D^{-1} = \begin{bmatrix} \mathbf{0}_{m \times m} & \sqrt{\frac{m}{n}}W \\ \sqrt{\frac{n}{m}}W^T & \mathbf{0}_{n \times n} \end{bmatrix}, \quad (13)$$

where \tilde{L} is from (8). Note that the eigenvectors of P are the eigenvectors ψ_k of \tilde{L} (see (10)) with corresponding eigenvalues $\mu_k = 1 - \lambda_k$, namely $\{\mu_1, \dots, \mu_{m+n}\} = \{1, s_2, \dots, s_m, 0, \dots, 0, -s_m, \dots, -s_2, -1\}$. Hence, the embedding (5) is given by the leading $q \leq m-1$ nontrivial eigenvectors of P with largest eigenvalues, which are always nonnegative. Recall that the sum of each row of W is $\sqrt{n/m}$ and the sum of each column is $\sqrt{m/n}$ (see (2)). Consequently, P is row-stochastic (i.e., the sum of each row of P is 1) and can be interpreted as the transition probability matrix of a random walk on the bipartite graph \mathcal{G} . At each step of this random walk, the random walker transitions from a node in \mathcal{X} to a node in \mathcal{Y} or vice versa according to the transition probability matrices $W\sqrt{m/n}$ or $W^T\sqrt{n/m}$, respectively. The transition probabilities after t consecutive steps of this random walk are given by the matrix

$$P^t = \begin{cases} \begin{bmatrix} P_{\mathcal{X}\mathcal{X}}^{(t)} & \mathbf{0}_{m \times n} \\ \mathbf{0}_{n \times m} & P_{\mathcal{Y}\mathcal{Y}}^{(t)} \end{bmatrix} & t \text{ is even,} \\ \begin{bmatrix} \mathbf{0}_{m \times m} & P_{\mathcal{X}\mathcal{Y}}^{(t)} \\ P_{\mathcal{Y}\mathcal{X}}^{(t)} & \mathbf{0}_{n \times n} \end{bmatrix} & t \text{ is odd,} \end{cases} \quad (14)$$

where

$$P_{\mathcal{X}\mathcal{X}}^{(t)} = US^tU^T, \quad P_{\mathcal{X}\mathcal{Y}}^{(t)} = \sqrt{\frac{m}{n}}US^tV^T, \quad P_{\mathcal{Y}\mathcal{Y}}^{(t)} = VS^tV^T, \quad P_{\mathcal{Y}\mathcal{X}}^{(t)} = \sqrt{\frac{n}{m}}VS^tU^T. \quad (15)$$

The matrices $P_{\mathcal{X}\mathcal{X}}^{(t)}$, $P_{\mathcal{X}\mathcal{Y}}^{(t)}$, $P_{\mathcal{Y}\mathcal{Y}}^{(t)}$, and $P_{\mathcal{Y}\mathcal{X}}^{(t)}$, which depend only on the transport plan W and its SVD, describe the probabilities to transition from a node in \mathcal{X} to a node in \mathcal{X} , a node in \mathcal{X} to a node in \mathcal{Y} , a node in \mathcal{Y} to a node in \mathcal{X} , and a node in \mathcal{Y} to a node in \mathcal{Y} , respectively, after t steps of the random walk. The i 'th row of P^t thus describes the probability distribution of the location of a random walker across all nodes of the graph after t steps of a walk that started at the i 'th node.

Given a graph over a set of data points, [15] proposed a robust approach to assess the similarity between any two points by initiating a random walk at these points and comparing the resulting distributions of the random walker's location after several steps. Specifically, [15] proposed to compute a weighted Euclidean distance between rows i and j of the random walk's transition probability matrix after t steps. This distance is termed the *diffusion distance* between the corresponding data points. We now construct a diffusion distance adapted to the random walk generated by P . This distance differs from the traditional diffusion distance proposed in [15] due to the bipartite nature of the graph \mathcal{G} and the fact that the resulting random walk is periodic.

Given a pair of points $x_i, x_{i'} \in \mathcal{X}$, we initiate random walks at these locations and assess the similarity between x_i and $x_{i'}$ by comparing the corresponding distributions of the random walker's location across \mathcal{X} for even t and across \mathcal{Y} for odd t (since the graph is bipartite). Specifically, we use the distance function

$$D_{\mathcal{X}}^{(t)}(x_i, x_{i'}) = \begin{cases} \sqrt{m} \left\| [P_{\mathcal{X}\mathcal{X}}^{(t)}]_{i,\cdot} - [P_{\mathcal{X}\mathcal{X}}^{(t)}]_{i',\cdot} \right\|_2, & t \text{ is even,} \\ \sqrt{n} \left\| [P_{\mathcal{X}\mathcal{Y}}^{(t)}]_{i,\cdot} - [P_{\mathcal{X}\mathcal{Y}}^{(t)}]_{i',\cdot} \right\|_2, & t \text{ is odd,} \end{cases} \quad (16)$$

where the notation $A_{i,\cdot}$ in (16) refers the i 'th row of a matrix A . Analogously, for a pair of points $y_j, y_{j'} \in \mathcal{Y}$, we use the distance function

$$D_{\mathcal{Y}}^{(t)}(y_j, y_{j'}) = \begin{cases} \sqrt{n} \left\| [P_{\mathcal{Y}\mathcal{Y}}^{(t)}]_{j,\cdot} - [P_{\mathcal{Y}\mathcal{Y}}^{(t)}]_{j',\cdot} \right\|_2, & t \text{ is even,} \\ \sqrt{m} \left\| [P_{\mathcal{Y}\mathcal{X}}^{(t)}]_{j,\cdot} - [P_{\mathcal{Y}\mathcal{X}}^{(t)}]_{j',\cdot} \right\|_2, & t \text{ is odd.} \end{cases} \quad (17)$$

To assess the similarity between a pair of points from distinct datasets, i.e., $x_i \in \mathcal{X}$ and $y_j \in \mathcal{Y}$, we have to account for the fact that $P_{i,\cdot}^{(t)}$ and $P_{m+j,\cdot}^{(t)}$ have disjoint supports for all t . Therefore, these random walk distributions cannot be directly compared using the traditional diffusion distance evaluated from P^t . Instead, we propose to use the distance functions

$$D_{\mathcal{X}\mathcal{Y}}^{(t)}(x_i, y_j) = \sqrt{n} \left\| \left[P_{\mathcal{X}\mathcal{Y}}^{(t)} \right]_{i,\cdot} - \left[P_{\mathcal{Y}\mathcal{Y}}^{(t)} \right]_{j,\cdot} \right\|_2, \quad (18)$$

$$D_{\mathcal{Y}\mathcal{X}}^{(t)}(y_j, x_i) = \sqrt{m} \left\| \left[P_{\mathcal{Y}\mathcal{X}}^{(t)} \right]_{j,\cdot} - \left[P_{\mathcal{X}\mathcal{X}}^{(t)} \right]_{i,\cdot} \right\|_2. \quad (19)$$

These distances essentially ignore the bipartite nature of the graph by directly comparing random walk distributions from P^t with different parities of t . We note that while the matrices $P_{\mathcal{X}\mathcal{X}}^{(t)}$, $P_{\mathcal{X}\mathcal{Y}}^{(t)}$, $P_{\mathcal{Y}\mathcal{X}}^{(t)}$, and $P_{\mathcal{Y}\mathcal{Y}}^{(t)}$ are always row-stochastic, they may not be nonnegative (entrywise) for all t . In particular, $P_{\mathcal{X}\mathcal{X}}^{(t)}$ and $P_{\mathcal{Y}\mathcal{Y}}^{(t)}$ ($P_{\mathcal{X}\mathcal{Y}}^{(t)}$ and $P_{\mathcal{Y}\mathcal{X}}^{(t)}$) are guaranteed to be nonnegative only for even (odd) values of t . Hence, we interpret $P_{\mathcal{X}\mathcal{X}}^{(t)}$ and $P_{\mathcal{Y}\mathcal{Y}}^{(t)}$ ($P_{\mathcal{X}\mathcal{Y}}^{(t)}$ and $P_{\mathcal{Y}\mathcal{X}}^{(t)}$) for odd (even) values of t as approximate transition probability matrices interpolated from their proper counterparts with even (odd) t . We now have the following proposition.

Proposition 3. *Let $q = m - 1$. Then, for any integer $t > 0$, we have*

$$\|\tilde{x}_i - \tilde{x}_{i'}\|_2 = D_{\mathcal{X}}^{(t)}(x_i, x_{i'}) = \sqrt{\sum_{k=2}^m s_k^{2t} (\sqrt{m}\mathbf{u}_k[i] - \sqrt{m}\mathbf{u}_k[i'])^2}, \quad (20)$$

$$\|\tilde{y}_j - \tilde{y}_{j'}\|_2 = D_{\mathcal{Y}}^{(t)}(y_j, y_{j'}) = \sqrt{\sum_{k=2}^m s_k^{2t} (\sqrt{n}\mathbf{v}_k[j] - \sqrt{n}\mathbf{v}_k[j'])^2}, \quad (21)$$

$$\|\tilde{x}_i - \tilde{y}_j\|_2 = D_{\mathcal{X}\mathcal{Y}}^{(t)}(x_i, y_j) = D_{\mathcal{Y}\mathcal{X}}^{(t)}(y_j, x_i) = \sqrt{\sum_{k=2}^m s_k^{2t} (\sqrt{m}\mathbf{u}_k[i] - \sqrt{n}\mathbf{v}_k[j])^2}, \quad (22)$$

for all $i, i' \in \{1, \dots, m\}$ and $j, j' \in \{1, \dots, n\}$, where \tilde{x}_i and \tilde{y}_j are from (5).

Proposition 3 shows that for the case of $q = m - 1$ and an integer $t > 0$, the Euclidean distance between any pair of points in the embedded data $\{\mathcal{X}, \mathcal{Y}\}$ is precisely the diffusion distance described in (16)–(19), which constitutes a proper metric over $\{\mathcal{X}, \mathcal{Y}\}$. This distance naturally encodes the similarities between the points in $\{\mathcal{X}, \mathcal{Y}\}$ according to the random walk generated by P after t steps. The main distinction here from the case of $t = 0$ is that all embedding coordinates in (5) are further weighted by powers of the corresponding singular values of W . Importantly, the decay of the coordinates' magnitudes becomes more rapid with more steps t in the random walk, and vice versa. Thus, according to (11), as t increases, the embedding in (5) emphasizes coordinates that are *more similar* between the datasets (i.e., associated with smaller eigenvalues λ_k) and attenuates coordinates that are more distinct.

While proposition 3 is stated for the embedding dimension $q = m - 1$, in practice we can discard embedding coordinates whose magnitude is sufficiently small, relying on the fact that s_k^{2t} decays rapidly with t for any $s_k < 1$. For instance, to approximate $\|\tilde{x}_i - \tilde{y}_j\|_2^2$ from Proposition 3 using the leading $q < m - 1$ coordinates of the embedding, we can take q such that the residual error

$$\sum_{k=q+1}^m s_k^{2t} (\sqrt{m}\mathbf{u}_k[i] - \sqrt{n}\mathbf{v}_k[j])^2 \leq (\sqrt{m} + \sqrt{n})^2 s_{q+1}^{2t}, \quad (23)$$

is smaller than a prescribed tolerance threshold. Similarly, we can approximate $\|\tilde{x}_i - \tilde{x}_{i'}\|_2^2$ and $\|\tilde{y}_j - \tilde{y}_{j'}\|_2^2$ using only q coordinates if $4ms_{q+1}^{2t}$ and $4ns_{q+1}^{2t}$ are smaller than the prescribed threshold, respectively. This approximation can achieve high accuracy with a relatively small embedding dimension q , even for a moderate number of steps t in the random walk.

3 Theoretical guarantees under a latent manifold model with distortions

In this section, we consider a setup where the points in each dataset are first sampled from a common latent manifold \mathcal{M} in a low-dimensional subspace \mathbb{R}^r and then embedded in a high-dimensional space \mathbb{R}^p with dataset-specific deformations and corruptions. We characterize the large-sample behavior of the matrices W and P from Section 2 in this setup and establish their convergence to certain analogous population quantities. We then investigate these population analogs and their spectral decompositions to justify our proposed approach.

Let $\bar{\mathcal{X}} = \{\bar{x}_1, \dots, \bar{x}_m\} \subset \mathbb{R}^r$ and $\bar{\mathcal{Y}} = \{\bar{y}_1, \dots, \bar{y}_n\} \subset \mathbb{R}^r$ be i.i.d samples from a probability measure $\omega(x)d\mu(x)$ supported on a d -dimensional compact Riemannian manifold $\mathcal{M} \subset \mathbb{R}^r$, where $\omega(x)$ is a positive and continuous probability density function on \mathcal{M} and $d\mu(x)$ is the volume form of \mathcal{M} at $x \in \mathcal{M}$. We consider $\bar{\mathcal{X}}$ and $\bar{\mathcal{Y}}$ as clean datasets containing latent variables of interest. The observed datasets $\mathcal{X} = \{x_1, \dots, x_m\} \subset \mathbb{R}^p$ and $\mathcal{Y} = \{y_1, \dots, y_n\} \subset \mathbb{R}^p$ are modeled as

$$x_i = \nu_1 + a_1 \mathcal{U} \bar{x}_i + \mathcal{V}_1 z_i^{(1)} + \eta_i^{(1)}, \quad y_j = \nu_2 + a_2 \mathcal{U} \bar{y}_j + \mathcal{V}_2 z_j^{(2)} + \eta_j^{(2)}, \quad (24)$$

for $i = 1, \dots, m$ and $j = 1, \dots, n$, where:

- $\nu_1, \nu_2 \in \mathbb{R}^p$ are arbitrary translation vectors;
- $a_1, a_2 > 0$ are arbitrary scaling factors;
- $\mathcal{U} \in \mathbb{R}^{p \times r}$ is a matrix with orthonormal columns representing a latent subspace shared between the datasets;
- $\mathcal{V}_1 \in \mathbb{R}^{p \times r_1}$ and $\mathcal{V}_2 \in \mathbb{R}^{p \times r_2}$ are matrices with orthonormal columns representing nuisance subspaces specific to each dataset, with $\mathcal{U}^T \mathcal{V}_1 = \mathbf{0}_{r \times r_1}$, $\mathcal{U}^T \mathcal{V}_2 = \mathbf{0}_{r \times r_2}$, and $\mathcal{V}_1^T \mathcal{V}_2 = \mathbf{0}_{r_1 \times r_2}$;
- $z_1^{(1)}, \dots, z_m^{(1)} \in \mathbb{R}^{r_1}$ and $z_1^{(2)}, \dots, z_n^{(2)} \in \mathbb{R}^{r_2}$ are arbitrary nuisance variables;
- $\eta_1^{(1)}, \dots, \eta_m^{(1)} \in \mathbb{R}^p$ and $\eta_1^{(2)}, \dots, \eta_n^{(2)} \in \mathbb{R}^p$ are data-specific sub-Gaussian random noise vectors (see [65]) with zero means, which are pairwise independent between the two datasets, namely $\eta_i^{(1)}$ and $\eta_j^{(2)}$ are independent for all i, j .

For a sub-Gaussian random vector $\eta \in \mathbb{R}^p$, we denote by $\|\eta\|_{\Psi_2} = \sup_{\|v\|_2=1} \|\eta^T v\|_{\Psi_2}$ its sub-Gaussian norm, where $\|\eta^T v\|_{\Psi_2}$ is the sub-Gaussian norm of the random variable $\eta^T v$; see [65]. We define the maximal sub-Gaussian norm among all noise vectors in (24) as $E := \max\{\|\eta_1^{(1)}\|_{\Psi_2}, \dots, \|\eta_m^{(1)}\|_{\Psi_2}, \|\eta_1^{(2)}\|_{\Psi_2}, \dots, \|\eta_n^{(2)}\|_{\Psi_2}\}$. We now make the following assumption on the boundedness of the quantities in the model (24).

Assumption 1. *There exist global constants $c, C > 0$ such that $\|\nu_1\|_2 \leq C$, $\|\nu_2\|_2 \leq C$, $c \leq a_1 \leq C$, $c \leq a_2 \leq C$, $\|z_i^{(1)}\|_2 \leq C$ for $i = 1, \dots, m$, $\|z_j^{(2)}\|_2 \leq C$ for $j = 1, \dots, n$, $\|x\|_2 \leq C$ for all $x \in \mathcal{M}$, and $E \leq C/(p^{1/4} \sqrt{\log p})$.*

According to Assumption 1, the magnitudes of the nuisance components in (24) are allowed to be comparable or even greater than the magnitudes of the latent variables on the manifold \mathcal{M} . The same is true of the magnitudes of the noise vectors $\eta_i^{(1)}$ and $\eta_j^{(2)}$. For example, consider $\eta_i^{(1)}, \eta_j^{(2)} \sim \mathcal{N}(\mathbf{0}_p, \Sigma^2)$, where $\Sigma^2 = I_p/(p^{1/2} \log p)$, which satisfies the condition on E in Assumption 1 (recalling that the sub-Gaussian norm of a Gaussian random vector is the largest eigenvalue of Σ up to a global constant; see [65]). Then, we have $\mathbb{E}\|\eta_i^{(1)}\|_2^2 = \mathbb{E}\|\eta_j^{(2)}\|_2^2 = \text{Trace}\{\Sigma^2\} = \sqrt{p}/\log p$, which is increasing in the ambient dimension p and can be arbitrarily large for high dimension, whereas the magnitudes of the latent variables are always upper bounded as $\|\bar{x}_i\|_2 \leq C$ and $\|\bar{y}_j\|_2 \leq C$. Note that the noise vectors $\eta_1^{(1)}, \dots, \eta_m^{(1)}$ and $\eta_1^{(2)}, \dots, \eta_n^{(2)}$ need not be identically distributed. Moreover, they are allowed to be dependent in each dataset separately. Similarly, the coordinates of each noise vector need not be identically distributed nor independent random variables. Hence, the noise distribution can significantly differ across the data and can be highly correlated between different coordinates and data points within each dataset. Such noise can adversely affect traditional

manifold learning and embedding techniques that operate on each dataset separately or on the concatenated data $\{\mathcal{X}, \mathcal{Y}\}$ [34]. Finally, we remark that the nuisance variables $\{z_i^{(1)}\}$ and $\{z_j^{(2)}\}$ need not have zero means, hence ν_1 and ν_2 are not necessarily the means of the observed points $\{x_i\}$ and $\{y_j\}$.

In addition to Assumption 1, we further assume that the ambient dimension p and the smaller dataset size m (recalling that $m \leq n$) are increasing with at least some fractional power of n .

Assumption 2. *There exists global constants $\kappa, \gamma > 0$ such that $\min\{p, m\} \geq \kappa n^\gamma$.*

Note that the size of the smaller dataset m and the ambient dimension p are allowed to grow very slowly with n , e.g., $m, p \sim n^{0.01}$, so they can practically be much smaller than n for large n . Alternatively, p can also grow much faster than m and n . The manifold \mathcal{M} and the quantities $d, \kappa, \gamma, c, C, \omega(x)$, are considered as fixed global constants in our setup. All constants appearing in our subsequent results may implicitly depend on these global constants. All other quantities are allowed to vary and can be arbitrary pending that they satisfy our assumptions. In particular, our results focus on the high-dimensional regime where m, n , and p are sufficiently large but are otherwise arbitrary.

To state our results, we define the kernels $\mathcal{W}_\varepsilon(x, y)$ and $\mathcal{K}_\varepsilon(x, y)$ as

$$\mathcal{W}_\varepsilon(x, y) = \rho_\varepsilon(x)\mathcal{K}_\varepsilon(x, y)\rho_\varepsilon(y), \quad \mathcal{K}_\varepsilon(x, y) = \frac{1}{(\pi\varepsilon)^{d/2}} \exp\left\{\frac{-\|x - y\|_2^2}{\varepsilon}\right\}, \quad (25)$$

for $x, y \in \mathcal{M}$, where $\rho_\varepsilon(x)$ is the function that solves the integral equation

$$\int_{\mathcal{M}} \mathcal{W}_\varepsilon(x, y)\omega(y)d\mu(y) = \int_{\mathcal{M}} \rho_\varepsilon(x)\mathcal{K}_\varepsilon(x, y)\rho_\varepsilon(y)\omega(y)d\mu(y) = 1, \quad (26)$$

for all $x \in \mathcal{M}$. In other words, $\mathcal{W}_\varepsilon(x, y)$ is obtained by symmetrically scaling the Gaussian kernel $\mathcal{K}_\varepsilon(x, y)$ to be doubly stochastic with respect to the measure $\omega d\mu$. The scaling function $\rho_\varepsilon(x)$ is guaranteed to exist and is a unique positive and continuous function on \mathcal{M} ; see [9] and [31]. We now have the following theorem regarding the population limit of the EOT plan, whose proof can be found in Appendix E.

Theorem 4. *Under Assumptions 1 and 2, there exist $\tau_0, n_0(\varepsilon), C'(\varepsilon) > 0$, such that for all $n \geq n_0(\varepsilon)$,*

$$|\sqrt{mn}W_{i,j} - \mathcal{W}_{\varepsilon/(a_1a_2)}(\bar{x}_i, \bar{y}_j)| \leq \tau C'(\varepsilon) \max\left\{E\sqrt{\log p}, E^2\sqrt{p\log p}, \sqrt{\frac{\log m}{m}}\right\}, \quad (27)$$

for all $i = 1, \dots, m$ and $j = 1, \dots, n$ with probability at least $1 - n^{-\tau}$, for all $\tau \geq \tau_0$.

Theorem 4 shows that under the latent manifold model (24), for any fixed bandwidth ε and sufficiently large m, n , and p , the entries of the transport plan $W_{i,j}$ concentrate around $(mn)^{-1/2}\mathcal{W}_{\varepsilon/(a_1a_2)}(\bar{x}_i, \bar{y}_j)$. We consider this quantity as the population analog of $W_{i,j}$. Note that the bandwidth parameter ε used to compute W (see (3)) is replaced here with the effective bandwidth $\varepsilon/(a_1a_2)$, where a_1 and a_2 are the factors scaling the two datasets in (24).

Theorem 4 provides a probabilistic bound on the error between $\sqrt{mn}W_{i,j}$ and $\mathcal{W}_{\varepsilon/(a_1a_2)}(\bar{x}_i, \bar{y}_j)$, which depends explicitly on m, p , and the sub-Gaussian norm of the noise E . If there is no noise, i.e., $E = 0$, then the probabilistic error converges almost surely to zero with a rate of $\sqrt{\log m/m}$, which describes sample-to-population convergence dominated by the smaller data dimension (recalling that $m \leq n$). In fact, in this case, we do not actually need the condition on the growth of the dimension p in Assumption 2. If noise is present, then the dominant error term depends on the behaviors of the quantities E, p , and m with respect to the large data dimension n . Importantly, under Assumptions 1 and 2, all error terms in the right-hand side of (36) must tend to zero as $n \rightarrow \infty$ for any fixed ε . Hence, $\sqrt{mn}W_{i,j}$ converges almost surely as $n \rightarrow \infty$ to $\mathcal{W}_{\varepsilon/(a_1a_2)}(\bar{x}_i, \bar{y}_j)$, which depends only on the locations of the latent variables \bar{x}_i and \bar{y}_j on the shared manifold \mathcal{M} , albeit using a different bandwidth that depends on a_1a_2 . Remarkably, this convergence holds despite the existence of arbitrary translations, orthogonal nuisance structures, and noise in the data, even if the noise is dependent between points in each dataset, non-identically distributed (heteroskedastic), and its magnitude grows unbounded with the dimension (see the text after Assumption 1).

Next, we provide geometric interpretation to our low-dimensional embedding by relating it to the eigenfunctions of suitable integral operators that encode the density and geometry of the shared manifold. Let \mathcal{L}_ω^2

be the Hilbert space of functions over \mathcal{M} endowed with the inner product $\langle g, h \rangle_\omega = \int_{\mathcal{M}} g(x)h(x)\omega(x)d\mu(x)$ for any $g, h : \mathcal{M} \rightarrow \mathbb{R}$. We define the integral operator $\mathcal{W}_\varepsilon : \mathcal{L}_\omega^2 \rightarrow \mathcal{L}_\omega^2$ via

$$\{\mathcal{W}_\varepsilon g\}(x) = \langle \mathcal{W}_\varepsilon(x, \cdot), g \rangle_\omega = \int_{\mathcal{M}} \mathcal{W}_\varepsilon(x, y)g(y)\omega(y)d\mu(y), \quad (28)$$

for all $x \in \mathcal{M}$ and any $g \in \mathcal{L}_\omega^2$. The integral operator \mathcal{W}_ε is compact, self-adjoint, and positive definite over \mathcal{L}_ω^2 [45], admitting a sequence of positive eigenvalues $\{\nu_k^{(\varepsilon)}\}_{k=1}^\infty$, sorted in descending order, and corresponding eigenfunctions $\{\xi_k^{(\varepsilon)}\}_{k=1}^\infty$, which are orthonormal and complete in \mathcal{L}_ω^2 . The first eigenpair of \mathcal{W}_ε is trivial, namely $\nu_1 = 1$ and $\xi_1(x) = 1$ for all $x \in \mathcal{M}$. Moreover, \mathcal{W}_ε is a transition probability operator with respect to the measure $\omega d\mu$, i.e., for any nonnegative function g satisfying $\int_{\mathcal{M}} g(y)\omega(y)d\mu(y) = 1$, we have that $\mathcal{W}_\varepsilon g$ is nonnegative and satisfies $\int_{\mathcal{M}} \{\mathcal{W}_\varepsilon g\}(x)\omega(x)d\mu(x) = 1$. Hence, \mathcal{W}_ε generates a random walk on the manifold \mathcal{M} , where $\mathcal{W}_\varepsilon^t g$ is the probability distribution of the random walker across \mathcal{M} after t steps of a random walk with the initial location distribution g .

We then define the Hilbert space $\mathcal{H} = \mathcal{L}_\omega^2 \times \mathcal{L}_\omega^2$, where each function $f \in \mathcal{H}$ can be written as $f = \begin{bmatrix} g \\ h \end{bmatrix}$ for $g, h \in \mathcal{L}_\omega^2$, endowed with the inner product $\langle f_1, f_2 \rangle_{\mathcal{H}} = \langle g_1, g_2 \rangle_\omega + \langle h_1, h_2 \rangle_\omega$ for any $f_1 = \begin{bmatrix} g_1 \\ h_1 \end{bmatrix}$ and $f_2 = \begin{bmatrix} g_2 \\ h_2 \end{bmatrix}$.

Additionally, we define the operator $\mathcal{P}_\varepsilon : \mathcal{H} \rightarrow \mathcal{H}$ such that for any $f = \begin{bmatrix} g \\ h \end{bmatrix} \in \mathcal{H}$,

$$\mathcal{P}_\varepsilon f = \begin{bmatrix} 0 & \mathcal{W}_\varepsilon \\ \mathcal{W}_\varepsilon & 0 \end{bmatrix} \begin{bmatrix} g \\ h \end{bmatrix} = \begin{bmatrix} \mathcal{W}_\varepsilon h \\ \mathcal{W}_\varepsilon g \end{bmatrix}. \quad (29)$$

The operator \mathcal{P}_ε is compact and self adjoint over \mathcal{H} , with eigenvalues $\{\nu_k^{(\varepsilon)}\}_{k=1}^\infty \cup \{-\nu_k^{(\varepsilon)}\}_{k=1}^\infty$ and corresponding eigenfunctions

$$\left\{ \frac{1}{\sqrt{2}} \begin{bmatrix} \xi_k^{(\varepsilon)} \\ \xi_k^{(\varepsilon)} \end{bmatrix} \right\}_{k=1}^\infty \cup \left\{ \frac{1}{\sqrt{2}} \begin{bmatrix} \xi_k^{(\varepsilon)} \\ -\xi_k^{(\varepsilon)} \end{bmatrix} \right\}_{k=1}^\infty, \quad (30)$$

which are orthonormal and complete in \mathcal{H} , where $\{\nu_k^{(\varepsilon)}\}$ and $\{\xi_k^{(\varepsilon)}\}$ are the eigenvalues and eigenfunctions of \mathcal{W}_ε , respectively. Since \mathcal{W}_ε is a transition probability operator over \mathcal{M} , then \mathcal{P}_ε is a transition probability operator over $\mathcal{M} \times \mathcal{M}$, describing a random walk between two copies of \mathcal{M} . At each step of this random walk, the random walker can transition from a location in one copy of the manifold to another location in the other copy, but not within the same copy of \mathcal{M} , akin to a random walk on a bipartite graph.

In what follows, for any $f = \begin{bmatrix} g \\ h \end{bmatrix} \in \mathcal{H}$, we define the evaluation of f at the pair of latent datasets $(\bar{\mathcal{X}}, \bar{\mathcal{Y}})$ as

$$[f]_{(\bar{\mathcal{X}}, \bar{\mathcal{Y}})} = \begin{bmatrix} [g]_{\bar{\mathcal{X}}} \\ [h]_{\bar{\mathcal{Y}}} \end{bmatrix} \quad [g]_{\bar{\mathcal{X}}} = \begin{bmatrix} g(\bar{x}_1) \\ \vdots \\ g(\bar{x}_m) \end{bmatrix}, \quad [h]_{\bar{\mathcal{Y}}} = \begin{bmatrix} h(\bar{y}_1) \\ \vdots \\ h(\bar{y}_n) \end{bmatrix}. \quad (31)$$

We now have the following corollary of Theorem 4, which establishes pointwise operator convergence of the matrix P from Section 2.3 (see (13)) to the integral operator $\mathcal{P}_{\varepsilon/(a_1 a_2)}$.

Corollary 5. *Fix an integer $t > 0$ and let $f = \begin{bmatrix} g \\ h \end{bmatrix} \in \mathcal{H}$, where g, h are bounded functions on \mathcal{M} . Then, under Assumptions 1 and 2, as $n \rightarrow \infty$, we have almost surely that*

$$\left\| P^t [f]_{(\bar{\mathcal{X}}, \bar{\mathcal{Y}})} - \left[\mathcal{P}_{\varepsilon/(a_1 a_2)}^t f \right]_{(\bar{\mathcal{X}}, \bar{\mathcal{Y}})} \right\|_\infty \rightarrow 0. \quad (32)$$

The proof of Corollary 5 can be found in Appendix F. Under the latent manifold model (24), Corollary 5 shows that applying the matrix P consecutively t times to any bounded function $f \in \mathcal{H}$ evaluated at the latent variables $(\bar{\mathcal{X}}, \bar{\mathcal{Y}})$, converges pointwise to the evaluated function obtained from applying the operator $\mathcal{P}_{\varepsilon/(a_1 a_2)}$ consecutively t times to f . This fact suggests that the random walk generated by P on the bipartite

graph \mathcal{G} (see Section 2.3) simulates a random walk between two copies of the manifold \mathcal{M} generated by the transition probability operator $\mathcal{P}_{\varepsilon/(a_1 a_2)}$. Let us elaborate on this connection. According to the definition of P in (13), we have $P = D^2 P^T D^{-2}$, where D is the diagonal matrix from (8). Hence, Corollary 5 asserts that for n large enough,

$$D^2 (P^T)^t D^{-2} [f]_{(\bar{\mathcal{X}}, \bar{\mathcal{Y}})} \sim \left[\mathcal{P}_{\varepsilon/(a_1 a_2)}^t f \right]_{(\bar{\mathcal{X}}, \bar{\mathcal{Y}})}. \quad (33)$$

Recall that $\mathcal{P}_{\varepsilon/(a_1 a_2)}$ is transition probability operator on $\mathcal{M} \times \mathcal{M}$ with respect to the measure $\omega d\mu \times \omega d\mu$. Therefore, if f is the initial location distribution of a random walker on $\mathcal{M} \times \mathcal{M}$, then the right-hand side of (33) is the location distribution of the random walker after t steps, evaluated at the locations of the combined latent dataset $(\bar{\mathcal{X}}, \bar{\mathcal{Y}})$. The left-hand side of (33) is a sample-based approximation to this evaluated probability distribution. Specifically, since P is a row-stochastic transition probability matrix, then for any probability vector $\mathbf{f} \in \mathbb{R}^{m+n}$ (i.e., with $\mathbf{f}[k] \geq 0$ and $\sum_k \mathbf{f}[k] = 1$) describing the initial location distribution of a random walker on the bipartite graph \mathcal{G} , the vector $(P^T)^t \mathbf{f}$ is a probability vector describing the location distribution of the random walker after t steps. In the left-hand side of (33), $(P^T)^t$ is applied to the vector $D^{-2} [f]_{(\bar{\mathcal{X}}, \bar{\mathcal{Y}})}$, which is the sample-based analog of the initial population-level distribution f (up to a scalar), where D^{-2} is used to normalize the entries of $[f]_{(\bar{\mathcal{X}}, \bar{\mathcal{Y}})}$ according to the sample sizes of \mathcal{X} and \mathcal{Y} (to compensate for a possible sample size imbalance). Finally, the multiplication by D^2 in (33) aims to undo the previous sample-based normalization. We thus consider the operator $\mathcal{P}_{\varepsilon/(a_1 a_2)}$ as the population analog of the matrix P under the latent manifold model.

Recall that our proposed embedding in Section 2 utilizes the leading nontrivial eigenvectors of P (which are also the eigenvectors of \tilde{L}) with large eigenvalues as coordinates of the combined embedded data $\{\tilde{\mathcal{X}}, \tilde{\mathcal{Y}}\}$; see (10). Motivated by Corollary 5, we propose to interpret our embedding via the eigenfunctions of the operator $\mathcal{P}_{\varepsilon/(a_1 a_2)}$. In this population interpretation, the leading nontrivial eigenfunctions of $\mathcal{P}_{\varepsilon/(a_1 a_2)}$ (see (30)) with positive eigenvalues are used to embed the coordinates of the data at the locations of the latent variables, i.e., the vector

$$\frac{1}{\sqrt{2}} \begin{bmatrix} \xi_k^{(\varepsilon/(a_1 a_2))} \\ \xi_k^{(\varepsilon/(a_1 a_2))} \end{bmatrix}_{(\bar{\mathcal{X}}, \bar{\mathcal{Y}})} = \frac{1}{\sqrt{2}} \begin{bmatrix} \xi_k^{(\varepsilon/(a_1 a_2))}(\bar{x}_1) \\ \vdots \\ \xi_k^{(\varepsilon/(a_1 a_2))}(\bar{x}_m) \\ \xi_k^{(\varepsilon/(a_1 a_2))}(\bar{y}_1) \\ \vdots \\ \xi_k^{(\varepsilon/(a_1 a_2))}(\bar{y}_n) \end{bmatrix}, \quad (34)$$

is the $(k-1)$ 'th coordinate of the embedded data up to a scalar multiple, for $k = 2, \dots, q+1 \leq m$, where $\xi_k^{(\varepsilon/(a_1 a_2))}(x)$ is the k 'th eigenfunction of $\mathcal{W}_{\varepsilon/(a_1 a_2)}$. Evidently, the entries of the vector (34) depend only on the locations of the underlying latent variables. Since the functions $\xi_k^{(\varepsilon/(a_1 a_2))}(x)$ are continuous on \mathcal{M} (as they are eigenfunctions of an integral operator with a continuous kernel on \mathcal{M}), the entries of (34) must be similar if their respective latent variables are sufficiently close on \mathcal{M} . This population interpretation suggests that under the latent manifold model (24) and for sufficiently large m , n , and p , our embedding from Section 2 aligns the two datasets according to the locations of their intrinsic latent variables on \mathcal{M} . That is, points x_i and y_j whose latent variables \bar{x}_i and \bar{y}_j are close on \mathcal{M} should be mapped to points \tilde{x}_i and \tilde{y}_j that are close in the embedding space \mathbb{R}^q .

Lastly, we discuss the behavior of the transport plan W and the operator $\mathcal{W}_{\varepsilon}$ for small bandwidth parameters. Under suitable conditions on the manifold \mathcal{M} and the density ω , the solution ρ_{ε} to the integral equation (25) satisfies $\rho_{\varepsilon}(x) \sim 1/\sqrt{\omega(x)}$ for small ε [33, 14, 68], and consequently $\mathcal{W}_{\varepsilon}(x, y) \sim \mathcal{K}_{\varepsilon}(x, y)/\sqrt{\omega(x)\omega(y)}$. Formally, we define the kernel

$$\hat{\mathcal{W}}_{\varepsilon}(x, y) = \frac{\mathcal{K}_{\varepsilon}(x, y)}{\sqrt{\omega(x)\omega(y)}}, \quad (35)$$

for all $x, y \in \mathcal{M}$. Combining Theorem 4 with the results of [33], we obtain the following corollary, whose proof can be found in Appendix G.

Corollary 6. *Suppose that Assumptions 1 and 2 hold, \mathcal{M} is smooth with no boundary, and $\omega \in \mathcal{C}^6(\mathcal{M})$. Then, there exist $\tau_0, \varepsilon_0, c', n_0(\varepsilon), C'(\varepsilon) > 0$, such that for all $n \geq n_0(\varepsilon)$ and $\varepsilon \leq \varepsilon_0$,*

$$\frac{1}{mn} \sum_{i,j} \left| \frac{\sqrt{mn}W_{i,j} - \hat{W}_{\varepsilon/(a_1 a_2)}(\bar{x}_i, \bar{y}_j)}{\hat{W}_{\varepsilon/(a_1 a_2)}(\bar{x}_i, \bar{y}_j)} \right| \leq c' \varepsilon + \tau C'(\varepsilon) \max \left\{ E\sqrt{\log p}, E^2\sqrt{p \log p}, \sqrt{\frac{\log m}{m}} \right\}, \quad (36)$$

with probability at least $1 - n^{-\tau}$, for all $\tau \geq \tau_0$.

Corollary 6 provides a bound on the relative error between $\sqrt{mn}W_{i,j}$ and $\hat{W}_{\varepsilon/(a_1 a_2)}(\bar{x}_i, \bar{y}_j)$, averaged over all $i = 1, \dots, m$ and $j = 1, \dots, n$. This bound consists of the sum of an $\mathcal{O}(\varepsilon)$ term and the same probabilistic error bound from Theorem 4, where the latter stems from the noise and the sample-to-population convergence. Overall, the error tends to zero almost surely if $m, n, p \rightarrow \infty$ sufficiently quickly while $\varepsilon \rightarrow 0$ sufficiently slowly. We note that the relative error used in Corollary 6 is more informative than the absolute error due to the rapid exponential decay of $\hat{W}_{\varepsilon}(x, y)$ as ε decreases. We conclude that under the latent manifold model, for small ε and sufficiently large m, n, p (depending on ε), the transport plan entries $W_{i,j}$ closely approximate $(mn)^{-1/2}\hat{W}_{\varepsilon/(a_1 a_2)}(\bar{x}_i, \bar{y}_j)$, which encodes the affinity between the latent variables \bar{x}_i and \bar{y}_j on \mathcal{M} via the Gaussian kernel normalized by the square roots of the sampling density at these locations.

Let us denote by $\mathscr{L}_{\varepsilon}$ the integral operator defined analogously to $\mathscr{W}_{\varepsilon}$ from (28) by replacing the kernel $W_{\varepsilon}(x, y)$ with $\hat{W}_{\varepsilon}(x, y)$ from (35). The operator $\mathscr{L}_{\varepsilon}$ and its discrete (sample-based) approximation are commonly employed for spectral clustering and manifold learning via the so-called symmetric normalized graph Laplacian; see, e.g., [67, 25, 27, 63] and references therein. In particular, using the latent dataset $\bar{\mathcal{X}}$, the (i, j) 'th entry of the symmetric normalized graph Laplacian is given by $\delta_{i,j} - \mathcal{K}_{\varepsilon}(\bar{x}_i, \bar{x}_j)/\sqrt{d_i d_j}$ for $i, j = 1, \dots, m$, where $d_i = \sum_k \mathcal{K}_{\varepsilon}(\bar{x}_i, \bar{x}_k)$ can be interpreted as a kernel density estimator that converges to the density $\omega(\bar{x}_i)$ for large m and small ε . The symmetric normalized graph Laplacian serves as a sample-based approximation to the population operator $\mathscr{L}_{\varepsilon} = \mathcal{I} - \mathscr{W}_{\varepsilon}$, where \mathcal{I} is the identity operator. For small ε , this operator is closely related to the differential operator Δ_{ω} defined by

$$\{\Delta_{\omega}g\}(x) = \frac{\Delta\{g\sqrt{\omega}\}(x)}{\sqrt{\omega(x)}} - \frac{\Delta\{\sqrt{\omega}\}(x)}{\sqrt{\omega(x)}}g(x), \quad (37)$$

for all $x \in \mathcal{M}$ and $g \in \mathcal{C}^2(\mathcal{M})$, where Δ is the negative Laplace-Beltrami (Laplacian) operator on \mathcal{M} [22]. Specifically, under suitable regularity conditions on \mathcal{M} and a sufficiently smooth function $g(x)$ on \mathcal{M} , we have the pointwise approximation $(4/\varepsilon)\{\mathscr{L}_{\varepsilon}g\}(x) = \{\Delta_{\omega}g\}(x) + \mathcal{O}(\varepsilon)$ [15, 25]. Moreover, spectral convergence (i.e., convergence of eigenvalues and eigenvectors) of $\mathscr{L}_{\varepsilon}$ to Δ_{ω} as $\varepsilon \rightarrow 0$ was established in [21]. We remark that spectral convergence to Δ_{ω} was also established directly for the operator $\mathscr{L}_{\varepsilon} = \mathcal{I} - \mathscr{W}_{\varepsilon}$ in the special case of a hyper-torus manifold [68].

Overall, our analysis suggests that under the latent manifold model (24), for sufficiently large m, n, p , and small ε , our proposed method approximates an embedding using the leading eigenfunctions of the operator Δ_{ω} evaluated at the combined latent dataset $\{\bar{X}, \bar{Y}\}$, irrespective of the deformations and corruptions. For a uniform sampling density on \mathcal{M} , i.e., if $\omega(x) = 1/\int_{\mathcal{M}} d\mu(y)$ for all $x \in \mathcal{M}$, the operator Δ_{ω} reduces to the standard manifold Laplacian Δ on \mathcal{M} . More generally, Δ_{ω} is the Fokker-Planck operator describing Brownian motion on \mathcal{M} via the Langevin equation [48]. The operator Δ_{ω} is self-adjoint and PSD, admitting a sequence of nonnegative eigenvalues $\{\tau_k\}_{k=1}^{\infty}$, sorted in ascending order, with corresponding eigenfunctions $\{\zeta_k\}_{k=1}^{\infty}$ that are orthonormal and complete in \mathcal{L}^2_{ω} . The first eigenpair of Δ_{ω} is trivial with $\tau_1 = 0$ and $\zeta_1(x) = 1$ for all $x \in \mathcal{M}$. The nontrivial eigenfunctions of Δ_{ω} simultaneously encode the sampling density ω and the intrinsic geometry of the manifold \mathcal{M} . Intuitively, smaller eigenvalues τ_k correspond to lower frequencies, namely smoother eigenfunctions $\zeta_k(x)$ with slower variation across regions of large density on \mathcal{M} [22]. The advantages of utilizing these eigenfunctions for clustering and manifold learning are well-established; see, e.g., [27, 63].

4 Simulation Studies

We evaluate the empirical performance of the proposed method EOT eigenmaps and its advantages over existing methods in terms of two analytical tasks. The first task is the alignment and joint embedding of

a pair of high-dimensional datasets, where the goal is to obtain a simultaneous low-dimensional embedding of both datasets in which the shared low-dimensional manifold structure is preserved and well-aligned. The second task is to obtain a joint clustering of all the data points in two datasets, which contain shared cluster patterns but also data-specific nuisance structures.

Noisy manifold alignment. We generate a pair of datasets $\{x_1, \dots, x_m\}$ and $\{y_1, \dots, y_n\}$ according to the latent manifold model (24). We consider two sets of simulation settings. In the first setting, we set

$$\mathcal{U} = \begin{bmatrix} \mathbf{I}_r \\ \mathbf{0} \end{bmatrix} \in \mathbb{R}^{p \times r}, \quad \mathcal{V}_1 = \mathbf{0}, \quad \mathcal{V}_2 = [\mathbf{e}_{r+1} \quad \mathbf{e}_{r+2} \quad \dots \quad \mathbf{e}_p] \in \mathbb{R}^{p \times (p-r)}, \quad (38)$$

where $\{\mathbf{e}_i\}$ is the ordinary Euclidean basis of \mathbb{R}^p . Setting $r = 3$, we sample the latent variables $\{\bar{x}_1, \dots, \bar{x}_m, \bar{y}_1, \dots, \bar{y}_n\} \in \mathbb{R}^r$ uniformly from a torus \mathbb{T} in \mathbb{R}^3 , so that

$$\{\bar{x}_1, \dots, \bar{x}_m, \bar{y}_1, \dots, \bar{y}_n\} \subset \mathbb{T} \equiv \{(2 + 0.8 \cos u) \cos v, (2 + 0.8 \cos u) \sin v, 0.8 \sin u) : u, v \in [0, 2\pi)\}. \quad (39)$$

We generate the observed datasets \mathcal{X} and \mathcal{Y} so that there is a global scale difference between them with various levels of mean shifts. Specifically, we set $z_i^{(1)} = z_i^{(2)} = 0$, $a_1 = 3\theta$, $a_2 = \theta$ for $\theta = 13$, and set $\nu_1 = \tau \cdot 3\theta \mathbf{e}_1 \in \mathbb{R}^p$ for different values of $\tau \in [1, 8]$, and $\nu_2 = \mathbf{0}$. Further, we generate homoskedastic noise so that $\eta_i^{(1)}$ and $\eta_i^{(2)}$ are independent multivariate Gaussian random vectors with mean 0 and covariance $\sigma^2 \mathbf{I}_p$ with $\sigma = 0.05\theta$. In the second setting, we fix $\tau = 1$ and generate data-specific nuisance structures by setting $z_i^{(1)} = 0$ for all i and by drawing each component of $z_i^{(2)} \in \mathbb{R}^{p-r}$ independently from a uniform distribution on $[\gamma\theta/2, \gamma\theta]$ for various levels of $\gamma \in [0, 1]$. We generate $\eta_i^{(1)} = [\eta_{i1}^{(1)}, \dots, \eta_{ip}^{(1)}]^T$ such that $\eta_{ik}^{(1)} \sim N(0, \sigma^2)$ and heteroskedastic noise $\eta_j^{(2)} = [\eta_{j1}^{(2)}, \dots, \eta_{jp}^{(2)}]^T$ such that

$$\eta_{jk}^{(2)} \sim \begin{cases} N(0, 10\sigma^2) & \text{if } 2 \leq k \leq r \text{ and } 1 \leq j \leq \lfloor \frac{n}{3} \rfloor \\ N(0, 5\sigma^2) & \text{if } 1 \leq k \leq r \text{ and } \frac{n}{3} < j \leq \lfloor \frac{2n}{3} \rfloor \\ N(0, \sigma^2) & \text{otherwise} \end{cases} \quad (40)$$

The other model parameters are the same as the first setting. Throughout our simulations, we set $n = m = 600$ and $p = 1000$. We set the embedding dimension $q = 3$.

We compare the following 9 methods in terms of both their embedding quality and alignment performance: (i) the proposed EOT eigenmaps with $t = 0$ (“EOT-0”); (ii) the proposed EOT eigenmaps with $t = 3$ (“EOT-1”); (iii) the landmark-based bipartite diffusion maps [51] (“lbdm”); (iv) the Seurat integration method [60] (“seurat”) whose implementation details are described in Appendix H; (v) the Roseland algorithm [56] (“rl”); (vi) PCA applied to each dataset separately, forming the q -dimensional embedding from the first q principle components, i.e., the first q eigenvectors of the sample covariance matrix of each dataset (“pca”); (vii) kernel-based PCA applied to each dataset separately, forming the q -dimensional embedding from the eigenvectors of the kernel matrix described in [19]; (viii) PCA applied to the concatenated dataset $\{x_1, \dots, x_m, y_1, \dots, y_n\}$, forming the embedding from the first q principle components (“j-pca”); (ix) kernel-based PCA applied to the concatenated dataset, forming the embedding from the first q eigenvectors of the kernel matrix described in [19] (“j-kpca”). For “EOT-0”, “EOT-1”, “lbdm” and “rl”, following the recommendation of [19], we set the bandwidth parameter ε for the corresponding kernel matrices as the median of all pairwise distances $\{\|x_i - y_j\|^2\}_{i \in [m], j \in [n]}$. To evaluate the performance of each method, we compare the obtained embedded data points $\tilde{T} = \{\tilde{x}_1, \dots, \tilde{x}_m, \tilde{y}_1, \dots, \tilde{y}_n\}$ to their corresponding latent variables $\bar{T} = \{\bar{x}_1, \dots, \bar{x}_m, \bar{y}_1, \dots, \bar{y}_n\}$ in terms of their local neighborhood structures. Specifically, for each $\mu \in \bar{T}$ and corresponding $\tilde{\mu} \in \tilde{T}$, we denote by S_μ the set of 50-nearest neighbors of μ in \bar{T} , and denote by W_μ the set of the 50-nearest neighbors of $\tilde{\mu}$ in \tilde{T} . We then compute the quantities

$$\text{concordance} = \frac{1}{m+n} \sum_{\mu \in \bar{T}} [\text{Jaccard Index}]_\mu, \quad [\text{Jaccard Index}]_\mu \equiv \frac{|S_\mu \cap W_\mu|}{|S_\mu \cup W_\mu|}, \quad (41)$$

where the denominator $(n+m)$ reflects the total number of data points. A higher concordance score suggests a better alignment of the two datasets in terms of the shared torus structure and a better recovery of the

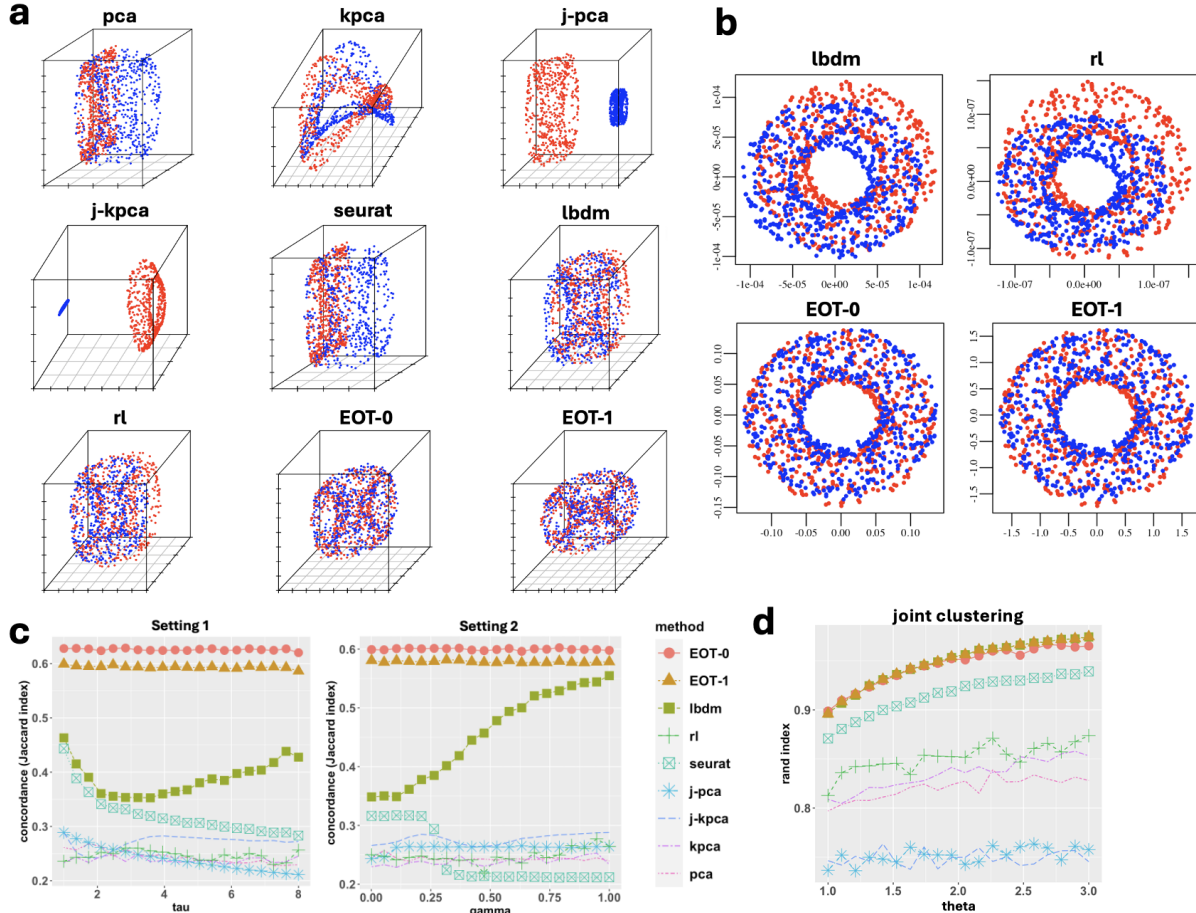


Figure 2: Comparison of nine integration methods based on simulations. (a) Visualization of the first three coordinates of each integrated low-dimensional embedding under Setting 1 of noisy manifold alignment experiments with $\tau = 8$, where the data points are colored according to datasets; (b) Closer comparison of the best four methods in (a) and (c) based on the first two coordinates of their integrated low-dimensional embeddings; (c) Numerical evaluation of different methods in terms of noisy manifold alignment across the two simulation settings; (d) Numerical evaluation of different methods in terms of joint clustering performance.

local neighborhood structure of the latent torus samples. For each setting, the simulation is repeated 500 times to calculate the averaged concordance.

We find that our proposed methods (“EOT-0” and “EOT-1”) in general have superior performance across all the settings over the alternative methods, with “EOT-0” slightly outperforming “EOT-1” (Figure 2a-c). Similar observations can be made under an alternative metric (i.e., Davies-Bouldin index, see Appendix H) focusing on the performance in alignment (Supplementary Figure S1 left and middle). As the magnitude of the mean shifts (τ) or the nuisance variable structures (γ) increases, the existing methods demonstrate poor to mediocre performance, whereas the proposed methods are significantly better and more robust (Figure 2c). From the visualization of the first three coordinates of each integrated low-dimensional embedding (Figure 2a) under Setting 1 with $\tau = 8$, we observe that most existing methods fail to capture and align the latent torus structures. Among the best four joint embedding methods indicated in Figure 2a, “lbdm” and “rl” achieve moderate performance in capturing the shared torus structure that is comparable with “EOT-0” and “EOT-1”, but a closer examination of the first two coordinates shows discernible misalignment of the two datasets by “lbdm” and “rl” (Figure 2b).

Joint clustering. Next, we consider the task of joint clustering of the samples in the two datasets, so that data points belonging to the same latent cluster are grouped together, even when they belong to distinct

datasets. Using the same notation as in the latent manifold model (24), we generate $\bar{x}_i, \bar{y}_i \in \mathbb{R}^r$, $r = 6$, from a Gaussian mixture model with 6 classes of equal proportions, where each Gaussian component has an identical covariance matrix \mathbf{I}_r , and the mean vector $\mu_j = 5\mathbf{e}_j$, $j = \{1, \dots, 6\}$, where $\{\mathbf{e}_j\}$ are the standard Euclidean basis in \mathbb{R}^r . The noises $\eta_{ik}^{(1)}$ are generated from $N(0, 1)$, whereas $\eta_{jk}^{(2)}$ are generated from (40) with $\sigma^2 = 1$. We set $\nu_1 = 15\mathbf{e}_1 + 15\mathbf{e}_2$, $\nu_2 = 0$, and $a_1 = a_2 = \theta$ for various values of $\theta \in [1, 3]$. We set $z_i^{(1)} = 0$, draw each component of $z_i^{(2)} \in \mathbb{R}^{p-r}$ independently from a uniform distribution on $[\theta/2, \theta]$, and set \mathcal{U} , \mathcal{V}_1 , \mathcal{V}_2 as in (38). In this way, both datasets contain a latent low-dimensional Gaussian mixture cluster structure with the common cluster centers, whereas discrepancies exist between the two datasets in terms of a mean shift, a nuisance structure, and heteroskedastic noises. We set $n = m = 600$ and $p = 1000$, and set the embedding dimension $q = 6$.

We compare the performance of nine different joint clustering algorithms, each corresponding to one of the joint embedding algorithms evaluated above, with an additional k -means algorithm ($k = 6$) applied to the integrated r -dimensional embeddings for both datasets. For each value of θ , we evaluate the clustering performance of each method using the Rand index [52] between the estimated and true cluster memberships. Specifically, suppose that \hat{M} and M are two partitions of $\{1, 2, \dots, n + m\}$ according to the estimated and true cluster memberships of all the samples, respectively. Then, the Rand index is defined as Rand index = $(a + b) / \binom{n+m}{2}$, where a is the number of pairs of elements in $\{1, 2, \dots, n + m\}$ that are in the same subset for both \hat{M} and M , and b is the number of pairs of elements that are in the different subsets for both \hat{M} and M . We repeat the simulation 500 times to calculate the averaged Rand index.

Figure 2d illustrates the behavior of the Rand index as a function of θ in our experiment, which controls the magnitudes of the latent variables and the nuisance structure. Evidently, as θ increases, all methods except for “j-pca” and “k-jpca” show improved clustering accuracy. Importantly, “EOT-0”, “EOT-1”, and “lbdm” exhibit superior performance in identifying the shared cluster patterns across the two datasets. In addition, we find that “EOT-0” and “EOT-1” perform significantly better than “lbdm” and the other methods in aligning the latent cluster patterns across datasets (Appendix Figure S1, rightmost panel).

5 Applications to Single-Cell Data Integration

We demonstrate two use cases of our method by analyzing several real-world single-cell omic datasets. In the first analysis, we aim to integrate several pairs of single-cell RNA-seq (scRNA-seq) datasets associated with different biological samples or experimental conditions in order to identify the common underlying cell types. In the second analysis, we integrate two different modalities (types of features) of single-cell data – gene expression data and chromatin accessibility data – for the same cells. The goal is to identify features in the two modalities that describe shared structures in the data.

Alignment of single-cell omics samples. We evaluate our methods on three integration tasks, where in each task we obtain joint embedding of a pair of single-cell omics datasets. The first pair of datasets concerns the human peripheral blood mononuclear cells (PBMCs) from lupus patients [29]. The PBMCs are split into two datasets, treated under different experimental conditions, and sequenced separately. In particular, $n_1 = 7451$ cells were treated with interferon beta, whereas the other $n_2 = 6548$ were untreated controls. The distinct experimental conditions and different sequencing batches necessarily introduced structural discrepancy, or batch effects, between the two datasets. Here we are interested in obtaining a joint embedding of all cells under both conditions into the same low-dimensional space, so as to align the corresponding cell types shared between the two datasets. We preprocess and normalize each dataset using the standard pipeline [19, 41] described in Appendix H and select the $p = 1000$ most variable genes for subsequent analysis. We apply our proposed method along with the seven alternative methods evaluated previously in our simulations. For each method, for various choices of q (from 2 to 20), we obtain a q -dimensional joint embedding of both datasets and then evaluate the embedding and alignment quality based on the following two metrics. The first metric is the Silhouette index (defined in Appendix H) with respect to the cell type annotations obtained from the previous scientific publication [29, 60]. The Silhouette index [53], calculated based on the pairwise distance matrix of the low-dimensional embeddings, measures the amount of discrepancy between the within-class distances and the inter-class distances with respect to a given sample, so that a higher value

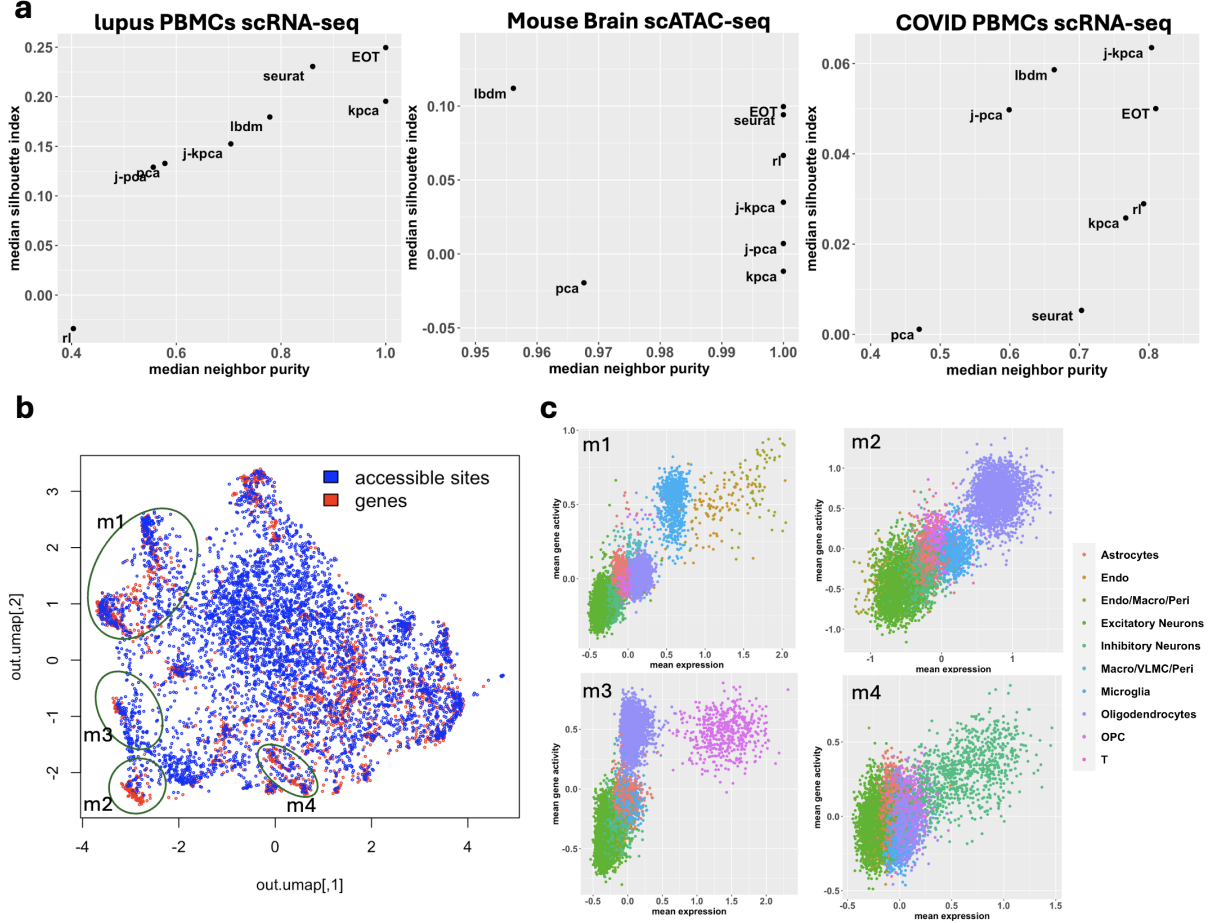


Figure 3: Integrative analyses of single-cell omics data. (a) Comparison of eight methods on three single-cell omics data integration tasks measured by two metrics, whose medians across a range of embedding dimensions q are shown here, where a higher value indicates better performance. (b) UMAP visualization of the joint low-dimensional embedding of genes and accessible chromatin regions, colored according to feature modalities. We select four clusters of features (m1-m4), identified by DBSCAN and each consisting of a regulatory module, for closer examination. (c) Scatter plots of the average expression (x-axis) of the genes and the average level of accessibility or gene activity (y-axis) of the accessible regions contained in each module for all the cells, where the cells are colored according to their cell type annotations.

indicates more significant separation of data points corresponding to distinct clusters. In our analysis, for each method and each q , we compute the mean Silhouette index across all the cells. The second metric is neighbor purity [40], which also quantifies the separation of cells in different cell types, but in a different way – by creating a hypersphere around each point in the cluster and computing the proportion of points in that hypersphere from the same cluster. For each method and each q , we compute the mean purity score across all cells in the embedding space.

Our second analysis concerns integrating a pair of single-cell ATAC-seq (scATAC-seq) datasets ($n_1 = 3618$ and $n_2 = 3715$) of mouse brain cells from different studies [39]. ATAC-seq is a biotechnology that quantifies genome-wide chromatin accessibility, which contains important information about epigenome dynamics and gene regulations. In our analysis, each dataset contains a matrix of ATAC-seq gene activity scores, characterizing gene-specific chromatin accessibility for individual cells. The third analysis concerns a pair of scRNA-seq datasets ($n_1 = 2839$ and $n_2 = 1221$) of human PBMCs from a COVID patient sampled from different time points after hospitalization [72]. For each pair of datasets, we perform the same analysis as before to obtain joint embeddings of all cells, followed by evaluating the Silhouette index and the neighbor purity score for each method. For the proposed method, in light of our previous simulation results, we consider the version

with $t = 0$. Figure 3a contains the evaluation results for the integrative analyses of all three pairs of datasets. For each analysis and each method, we present the median of the two metrics across different embedding dimensions q in a scatter plot. The more detailed results concerning the metric scores for all the q values are summarized as boxplots in Supplementary Figure S2. To compare different methods we will focus on the relative magnitude of these metrics for given integration task, since their absolute magnitude would partially depend on the cell type proportions; for example, for the mouse brain scATAC-seq data, the neighbor purity is close to 1 for all methods since there are more than 50% of cells under the same cell type “Excitatory Neurons.” Our results indicate that our proposed method exhibits overall the best performance in terms of both metrics, staying at the right upper corner of each scatter plot, whereas the alternative methods have varying performance across the three analytical tasks. Moreover, the proposed approach is robust to the choice of the embedding dimension q , performing well across a wide range of embedding dimensions.

Inferring simultaneous accessibility-expression modules. We consider the joint analysis of simultaneous profiling of gene expression and chromatin accessibility of human prefrontal cortex (PFC) cells generated from the Single Cell Opioid Responses in the Context of HIV (SCORCH) Study [2]. Specifically, We examined a dataset for a PFC sample of an HIV patient containing $n = 7534$ cells, generated from the 10X Multiome technology capturing concurrent measurements of gene expression profiles via single nucleus RNA sequencing (snRNA-seq) and chromatin accessibility landscapes within individual cells. We focused on a selection of chromatin accessibility regions proximal to gene promoters. The degree of chromatin openness in these promoter regions is indicative of the corresponding gene’s activity level. For the gene expression data, we select $p_1 = 2000$ most variable genes, whereas for the chromatin accessibility data, we select $p_2 = 5000$ most variably accessible regions. Our goal is to obtain a joint embedding of all the $p_1 + p_2$ features from both modalities into the same low-dimensional space, so as to identify associations between chromatin accessible regions and genes. Unlike many existing methods that focus on linear correlations between the features [30, 10], our method is expected to further capture nonlinear relationships between chromatin accessibility and gene expression, which are likely more prominent in biological organisms [42]. Note that in this analysis we have the registered cells between the two datasets but different features. To obtain joint embeddings of the features, we apply our proposed method by reversing the roles of cells and features. Additional implementation details are provided in Appendix H.

Figure 3b contains a UMAP visualization [6] of the obtained joint embedding, where the embedding dimension $r = 34$ is determined based on thresholding the eigengap (Appendix H). The closeness of features in the joint embedding space, or in the UMAP visualization, indicates a higher association between their values across the cell population. The UMAP visualization reveals clusters of features, with many clusters containing both genes and accessible chromatin regions. We interpret these clusters as simultaneous accessibility-expression regulatory modules. Specifically, each module consists of a group of correlated (co-accessible) chromatin accessible regions and a group of correlated (co-expressed) genes, which are mutually associated to each other, possibly as a result of some shared regulatory pathways. To further examine the relationship between the associated accessible sites and the genes, we choose as examples four different modules (m1-m4), indicated in Figure 3b, that are identified by the DBSCAN algorithm [24] based on our joint embeddings (Supplementary Figure S3). Figure 3c contains the scatter plots of the average expression (x-axis) of the genes and the average level of accessibility or gene activity (y-axis) of the accessible regions contained in each module for all the cells, where the cells are colored according to their cell type annotations. We observe that, for each module, there exists at least one cell type that demonstrates a higher expression level for the genes in the module, and/or a higher accessibility level for the chromatin regions in the same module, as compared with other cell types. For example, module m2 contains 133 genes and 31 accessible regions, whose average values are simultaneously higher in oligodendrocytes as compared with other cell types; module m4 contains 109 genes and 81 accessible regions, whose average values are simultaneously higher in inhibitory neurons as compared with other cell types. Interestingly, in module m3, both oligodendrocytes and OPCs have higher average values for the 33 accessible regions, whereas only OPCs have higher expression level for the 133 genes in m3, indicating the cell-type-specific nature of gene regulation. These analyses, made possible by our joint feature embedding, are useful for characterizing the interaction between epigenomic dynamics and transcription, and for understanding the gene regulation heterogeneity across cell types.

6 Summery and discussion

In this work, we proposed a principled approach to align and jointly embed two datasets \mathcal{X} and \mathcal{Y} via the leading singular vectors of their EOT plan W . We showed that our approach can be interpreted as an inter-data variant of the classical Laplacian eigenmaps and diffusion maps embeddings for a single dataset, where our approach enjoys many favorable properties analogous to these methods. Furthermore, we provided theoretical guarantees for our method under a latent manifold model with distortions in a high-dimensional regime, establishing connections between our embedding and certain population operators that encode the manifold’s density and geometry. Finally, we demonstrated the superior performance of our technique over alternative methods in simulations and real data.

Our results suggest several possible future research directions. Firstly, it is desirable to extend our approach beyond the case of two datasets, namely, when the goal is to align and jointly embed an arbitrary number of datasets simultaneously. One potential approach is to consider all possible transport plans between pairs of datasets. However, it is not immediately obvious how to obtain a joint embedding from all pairwise transport plans and what are the interpretations and analytical properties of such an embedding. Another direction of interest is to allow for variable bandwidth kernels [8] beyond a single bandwidth parameter ε . Several variants of optimal transport were recently proposed to account for this [64, 46]. Such extensions can better adapt to local variations in the sampling density and further automate the embedding procedure. However, these approaches require substantial analytical and numerical investigation from the perspective of alignment and joint embedding under deformations and corruptions. Finally, it is desirable to expand the theoretical results of Section 3 by considering more general deformation models and establishing more refined analytical results, e.g., pointwise error rates that depend explicitly on ε and spectral convergence guarantees. We leave such extensions for future work.

7 Acknowledgements

BL and YK acknowledge funding support from NIH grants R01GM131642, UM1PA051410, R33DA047037, U54AG076043, U54AG079759, U01DA053628, P50CA121974, and R01GM135928. RM would like to thank Xiucui Ding, Jason Buenrostro, Rafael Irizarry, and Chang Lu for their helpful discussions.

References

- [1] Zeyuan Allen-Zhu, Yuanzhi Li, Rafael Oliveira, and Avi Wigderson. Much faster algorithms for matrix scaling. In *2017 IEEE 58th Annual Symposium on Foundations of Computer Science (FOCS)*, pages 890–901. IEEE, 2017.
- [2] Seth A Ament, Rianne R Campbell, Mary Kay Lobo, Joseph P Receveur, Kriti Agrawal, Alejandra Borjabad, Siddappa N Byrareddy, Linda Chang, Declan Clarke, Prashant Emani, et al. The single-cell opioid responses in the context of hiv (scorch) consortium. *Molecular Psychiatry*, pages 1–12, 2024.
- [3] Sindri E Antonsson and Páll Melsted. Batch correction methods used in single cell rna-sequencing analyses are often poorly calibrated. *bioRxiv*, pages 2024–03, 2024.
- [4] Ricard Argelaguet, Damien Arnot, Danila Bredikhin, Yonatan Deloro, Britta Velten, John C Marioni, and Oliver Stegle. Mofa+: a statistical framework for comprehensive integration of multi-modal single-cell data. *Genome biology*, 21:1–17, 2020.
- [5] Ricard Argelaguet, Anna SE Cuomo, Oliver Stegle, and John C Marioni. Computational principles and challenges in single-cell data integration. *Nature biotechnology*, 39(10):1202–1215, 2021.
- [6] Etienne Becht, Leland McInnes, John Healy, Charles-Antoine Dutertre, Immanuel WH Kwok, Lai Guan Ng, Florent Ginhoux, and Evan W Newell. Dimensionality reduction for visualizing single-cell data using umap. *Nature biotechnology*, 37(1):38–44, 2019.
- [7] Mikhail Belkin and Partha Niyogi. Laplacian eigenmaps for dimensionality reduction and data representation. *Neural computation*, 15(6):1373–1396, 2003.

- [8] Tyrus Berry and John Harlim. Variable bandwidth diffusion kernels. *Applied and Computational Harmonic Analysis*, 40(1):68–96, 2016.
- [9] Jonathan M Borwein, Adrian Stephen Lewis, and Roger D Nussbaum. Entropy minimization, dad problems, and doubly stochastic kernels. *Journal of Functional Analysis*, 123(2):264–307, 1994.
- [10] Carmen Bravo González-Blas, Seppe De Winter, Gert Hulselmans, Nikolai Hecker, Irina Matetovici, Valerie Christiaens, Suresh Poovathingal, Jasper Wouters, Sara Aibar, and Stein Aerts. Scenic+: single-cell multiomic inference of enhancers and gene regulatory networks. *Nature Methods*, 20(9):1355–1367, 2023.
- [11] Kai Cao, Qiyu Gong, Yiguang Hong, and Lin Wan. A unified computational framework for single-cell data integration with optimal transport. *Nature Communications*, 13(1):7419, 2022.
- [12] Guillaume Carlier, Vincent Duval, Gabriel Peyré, and Bernhard Schmitzer. Convergence of entropic schemes for optimal transport and gradient flows. *SIAM Journal on Mathematical Analysis*, 49(2):1385–1418, 2017.
- [13] Tara Chari and Lior Pachter. The specious art of single-cell genomics. *PLOS Computational Biology*, 19(8):e1011288, 2023.
- [14] Xiuyuan Cheng and Boris Landa. Bi-stochastically normalized graph laplacian: convergence to manifold laplacian and robustness to outlier noise. *arXiv preprint arXiv:2206.11386*, 2022.
- [15] Ronald R Coifman and Stéphane Lafon. Diffusion maps. *Applied and computational harmonic analysis*, 21(1):5–30, 2006.
- [16] Marco Cuturi. Sinkhorn distances: Lightspeed computation of optimal transport. In *Advances in neural information processing systems*, pages 2292–2300, 2013.
- [17] Umeshwar Dayal, Malu Castellanos, Alkis Simitsis, and Kevin Wilkinson. Data integration flows for business intelligence. In *Proceedings of the 12th International Conference on Extending Database Technology: Advances in Database Technology*, pages 1–11, 2009.
- [18] Pinar Demetci, Rebecca Santorella, Björn Sandstede, William Stafford Noble, and Ritambhara Singh. Scot: single-cell multi-omics alignment with optimal transport. *Journal of computational biology*, 29(1):3–18, 2022.
- [19] Xiukai Ding and Rong Ma. Learning low-dimensional nonlinear structures from high-dimensional noisy data: an integral operator approach. *The Annals of Statistics*, 51(4):1744–1769, 2023.
- [20] Xiukai Ding and Rong Ma. Kernel spectral joint embeddings for high-dimensional noisy datasets using duo-landmark integral operators. *arXiv preprint arXiv:2405.12317*, 2024.
- [21] Nicolás García Trillos, Moritz Gerlach, Matthias Hein, and Dejan Slepčev. Error estimates for spectral convergence of the graph laplacian on random geometric graphs toward the laplace–beltrami operator. *Foundations of Computational Mathematics*, 20(4):827–887, 2020.
- [22] Alexander Grigor’yan. Heat kernels on weighted manifolds and applications. *Cont. Math*, 398(2006):93–191, 2006.
- [23] Laleh Haghverdi, Aaron TL Lun, Michael D Morgan, and John C Marioni. Batch effects in single-cell rna-sequencing data are corrected by matching mutual nearest neighbors. *Nature biotechnology*, 36(5):421–427, 2018.
- [24] Michael Hahsler, Matthew Piekenbrock, and Derek Doran. dbscan: Fast density-based clustering with r . *Journal of Statistical Software*, 91:1–30, 2019.
- [25] Matthias Hein, Jean-Yves Audibert, and Ulrike von Luxburg. Graph laplacians and their convergence on random neighborhood graphs. *Journal of Machine Learning Research*, 8(6), 2007.
- [26] Brian Hie, Bryan Bryson, and Bonnie Berger. Efficient integration of heterogeneous single-cell transcriptomes using scanorama. *Nature biotechnology*, 37(6):685–691, 2019.

- [27] Franca Hoffmann, Bamdad Hosseini, Assad A Oberai, and Andrew M Stuart. Spectral analysis of weighted laplacians arising in data clustering. *Applied and Computational Harmonic Analysis*, 56:189–249, 2022.
- [28] Roger A Horn, Roger A Horn, and Charles R Johnson. *Topics in matrix analysis*. Cambridge university press, 1994.
- [29] Hyun Min Kang, Meena Subramaniam, Sasha Targ, Michelle Nguyen, Lenka Maliskova, Elizabeth McCarthy, Eunice Wan, Simon Wong, Lauren Byrnes, Cristina M Lanata, et al. Multiplexed droplet single-cell rna-sequencing using natural genetic variation. *Nature biotechnology*, 36(1):89–94, 2018.
- [30] Vinay K Kartha, Fabiana M Duarte, Yan Hu, Sai Ma, Jennifer G Chew, Caleb A Lareau, Andrew Earl, Zach D Burkett, Andrew S Kohlway, Ronald Lebofsky, et al. Functional inference of gene regulation using single-cell multi-omics. *Cell genomics*, 2(9), 2022.
- [31] Paul Knopp and Richard Sinkhorn. A note concerning simultaneous integral equations. *Canadian Journal of Mathematics*, 20:855–861, 1968.
- [32] Boris Landa. Scaling positive random matrices: concentration and asymptotic convergence. *Electronic Communications in Probability*, 27:1–13, 2022.
- [33] Boris Landa and Xiuyuan Cheng. Robust inference of manifold density and geometry by doubly stochastic scaling. *SIAM Journal on Mathematics of Data Science*, 5(3):589–614, 2023.
- [34] Boris Landa, Ronald R Coifman, and Yuval Kluger. Doubly stochastic normalization of the gaussian kernel is robust to heteroskedastic noise. *SIAM journal on mathematics of data science*, 3(1):388–413, 2021.
- [35] Xiangjie Li, Kui Wang, Yafei Lyu, Huize Pan, Jingxiao Zhang, Dwight Stambolian, Katalin Susztak, Muredach P Reilly, Gang Hu, and Mingyao Li. Deep learning enables accurate clustering with batch effect removal in single-cell rna-seq analysis. *Nature communications*, 11(1):2338, 2020.
- [36] Tianyi Lin, Nhat Ho, and Michael I Jordan. On the efficiency of entropic regularized algorithms for optimal transport. *Journal of Machine Learning Research*, 23(137):1–42, 2022.
- [37] Jialin Liu, Chao Gao, Joshua Sodicoff, Velina Kozareva, Evan Z Macosko, and Joshua D Welch. Jointly defining cell types from multiple single-cell datasets using liger. *Nature protocols*, 15(11):3632–3662, 2020.
- [38] Romain Lopez, Jeffrey Regier, Michael B Cole, Michael I Jordan, and Nir Yosef. Deep generative modeling for single-cell transcriptomics. *Nature methods*, 15(12):1053–1058, 2018.
- [39] Malte D Luecken, Maren Büttner, Kridsakorn Chaichoompu, Anna Danese, Marta Interlandi, Michaela F Müller, Daniel C Strobl, Luke Zappia, Martin Dugas, Maria Colomé-Tatché, et al. Benchmarking atlas-level data integration in single-cell genomics. *Nature methods*, 19(1):41–50, 2022.
- [40] A Lun. bluster: Clustering algorithms for bioconductor. r package version 1.15.0. *Bioconductor*, 2022.
- [41] Rong Ma, Eric D Sun, David Donoho, and James Zou. Principled and interpretable alignability testing and integration of single-cell data. *Proceedings of the National Academy of Sciences*, 121(10):e2313719121, 2024.
- [42] Sai Ma, Bing Zhang, Lindsay M LaFave, Andrew S Earl, Zachary Chiang, Yan Hu, Jiarui Ding, Alison Brack, Vinay K Kartha, Tristan Tay, et al. Chromatin potential identified by shared single-cell profiling of rna and chromatin. *Cell*, 183(4):1103–1116, 2020.
- [43] Hassaan Maan, Lin Zhang, Chengxin Yu, Michael J Geuenich, Kieran R Campbell, and Bo Wang. Characterizing the impacts of dataset imbalance on single-cell data integration. *Nature Biotechnology*, pages 1–10, 2024.
- [44] Laurens van der Maaten and Geoffrey Hinton. Visualizing data using t-sne. *Journal of machine learning research*, 9(Nov):2579–2605, 2008.

- [45] Nicholas F Marshall and Ronald R Coifman. Manifold learning with bi-stochastic kernels. *IMA Journal of Applied Mathematics*, 84(3):455–482, 2019.
- [46] Tetsuya Matsumoto, Stephen Zhang, and Geoffrey Schiebinger. Beyond knn: Adaptive, sparse neighborhood graphs via optimal transport. *arXiv preprint arXiv:2208.00604*, 2022.
- [47] Gonzalo Mena and Jonathan Niles-Weed. Statistical bounds for entropic optimal transport: sample complexity and the central limit theorem. *Advances in neural information processing systems*, 32, 2019.
- [48] Boaz Nadler, Stéphane Lafon, Ronald R Coifman, and Ioannis G Kevrekidis. Diffusion maps, spectral clustering and reaction coordinates of dynamical systems. *Applied and Computational Harmonic Analysis*, 21(1):113–127, 2006.
- [49] Marcel Nutz and Johannes Wiesel. Entropic optimal transport: Convergence of potentials. *Probability Theory and Related Fields*, 184(1):401–424, 2022.
- [50] Gabriel Peyré, Marco Cuturi, et al. Computational optimal transport: With applications to data science. *Foundations and Trends® in Machine Learning*, 11(5-6):355–607, 2019.
- [51] Khiem Pham and Guangliang Chen. Large-scale spectral clustering using diffusion coordinates on landmark-based bipartite graphs. In *Proceedings of the Twelfth Workshop on Graph-Based Methods for Natural Language Processing (TextGraphs-12)*, pages 28–37, 2018.
- [52] William M Rand. Objective criteria for the evaluation of clustering methods. *Journal of the American Statistical association*, 66(336):846–850, 1971.
- [53] Peter J Rousseeuw. Silhouettes: a graphical aid to the interpretation and validation of cluster analysis. *Journal of computational and applied mathematics*, 20:53–65, 1987.
- [54] Uri Shaham, Kelly P Stanton, Jun Zhao, Huamin Li, Khadir Raddassi, Ruth Montgomery, and Yuval Kluger. Removal of batch effects using distribution-matching residual networks. *Bioinformatics*, 33(16):2539–2546, 2017.
- [55] Micah J Sheller, Brandon Edwards, G Anthony Reina, Jason Martin, Sarthak Pati, Aikaterini Kotrotsou, Mikhail Milchenko, Weilin Xu, Daniel Marcus, Rivka R Colen, et al. Federated learning in medicine: facilitating multi-institutional collaborations without sharing patient data. *Scientific reports*, 10(1):12598, 2020.
- [56] Chao Shen and Hau-Tieng Wu. Scalability and robustness of spectral embedding: landmark diffusion is all you need. *Information and Inference: A Journal of the IMA*, 11(4):1527–1595, 2022.
- [57] Richard Sinkhorn. A relationship between arbitrary positive matrices and doubly stochastic matrices. *The Annals of Mathematical Statistics*, 35(2):876–879, 1964.
- [58] Richard Sinkhorn. Diagonal equivalence to matrices with prescribed row and column sums. *The American Mathematical Monthly*, 74(4):402–405, 1967.
- [59] Richard Sinkhorn and Paul Knopp. Concerning nonnegative matrices and doubly stochastic matrices. *Pacific Journal of Mathematics*, 21(2):343–348, 1967.
- [60] Tim Stuart, Andrew Butler, Paul Hoffman, Christoph Hafemeister, Efthymia Papalexi, William M Mauck, Yuhan Hao, Marlon Stoeckius, Peter Smibert, and Rahul Satija. Comprehensive integration of single-cell data. *cell*, 177(7):1888–1902, 2019.
- [61] Tim Stuart and Rahul Satija. Integrative single-cell analysis. *Nature reviews genetics*, 20(5):257–272, 2019.
- [62] Hoa Thi Nhu Tran, Kok Siong Ang, Marion Chevrier, Xiaomeng Zhang, Nicole Yee Shin Lee, Michelle Goh, and Jinmiao Chen. A benchmark of batch-effect correction methods for single-cell rna sequencing data. *Genome biology*, 21:1–32, 2020.
- [63] Nicolás García Trillos, Franca Hoffmann, and Bamdad Hosseini. Geometric structure of graph laplacian embeddings. *J. Mach. Learn. Res.*, 22:63–1, 2021.

- [64] Hugues Van Assel, Titouan Vayer, Rémi Flamary, and Nicolas Courty. Snekhorn: Dimension reduction with symmetric entropic affinities. *Advances in Neural Information Processing Systems*, 36, 2024.
- [65] Roman Vershynin. *High-dimensional probability: An introduction with applications in data science*, volume 47. Cambridge university press, 2018.
- [66] Cédric Villani et al. *Optimal transport: old and new*, volume 338. Springer, 2009.
- [67] Ulrike Von Luxburg. A tutorial on spectral clustering. *Statistics and computing*, 17(4):395–416, 2007.
- [68] Caroline L Wormell and Sebastian Reich. Spectral convergence of diffusion maps: Improved error bounds and an alternative normalization. *SIAM Journal on Numerical Analysis*, 59(3):1687–1734, 2021.
- [69] B Yu and K Kumbier. Veridical data science. *Proceedings of the National Academy of Sciences of the United States of America*, 117(8):3920–3929, 2020.
- [70] Bin Yu and Rebecca Barter. The data science process: One culture. *Journal of the American Statistical Association*, 115(530):672–674, 2020.
- [71] Ron Zass and Amnon Shashua. Doubly stochastic normalization for spectral clustering. In *Advances in neural information processing systems*, pages 1569–1576, 2007.
- [72] Linnan Zhu, Penghui Yang, Yingze Zhao, Zhenkun Zhuang, Zhifeng Wang, Rui Song, Jie Zhang, Chuanyu Liu, Qianqian Gao, Qumiao Xu, et al. Single-cell sequencing of peripheral mononuclear cells reveals distinct immune response landscapes of covid-19 and influenza patients. *Immunity*, 53(3):685–696, 2020.

Appendix A Proof of Proposition 1

Under the constraints (7), the objective function (6) can be simplified as

$$\begin{aligned}
J(\mathcal{X}', \mathcal{Y}') &= \sum_i \|x'_i\|_2^2 \sum_j W_{i,j} + \sum_j \|y'_j\|_2^2 \sum_i W_{i,j} - 2 \sum_{i,j} \left((x'_i)^T y'_j \right) W_{i,j} \\
&= 2q\sqrt{mn} - 2 \sum_{i,j} \left((x'_i)^T y'_j \right) W_{i,j} = 2q\sqrt{mn} - 2 \sum_{k=1}^q \left[x'_1[k], \dots, x'_m[k] \right] W \left[y'_1[k], \dots, y'_n[k] \right]^T,
\end{aligned} \tag{42}$$

where we used the fact that $W \in \mathcal{B}_{m,n}$. By the properties of the SVD and the fact that the first pair of singular vectors of W is trivial (see text after (4)), it follows that taking $\left[x'_1[k], \dots, x'_m[k] \right]^T = \sqrt{m}\mathbf{u}_k$ and $\left[y'_1[k], \dots, y'_n[k] \right]^T = \sqrt{n}\mathbf{v}_k$ for $k = 2, \dots, q \leq m - 1$ minimizes (42) under the constraints (7).

Appendix B Proof of Proposition 2

To prove the first part of Proposition 2, it can be verified directly that the vectors

$$\begin{aligned}
\{\phi_1, \dots, \phi_{m+n}\} &= \left\{ \begin{bmatrix} \frac{1}{\sqrt{2m}} \mathbf{1}_m \\ \frac{1}{\sqrt{2n}} \mathbf{1}_n \end{bmatrix}, \begin{bmatrix} \frac{1}{\sqrt{2}} \mathbf{u}_2 \\ \frac{1}{\sqrt{2}} \mathbf{v}_2 \end{bmatrix}, \dots, \begin{bmatrix} \frac{1}{\sqrt{2}} \mathbf{u}_m \\ \frac{1}{\sqrt{2}} \mathbf{v}_m \end{bmatrix}, \right. \\
&\quad \left. \begin{bmatrix} \mathbf{0}_m \\ \mathbf{v}_{m+1} \end{bmatrix}, \dots, \begin{bmatrix} \mathbf{0}_m \\ \mathbf{v}_{m+n} \end{bmatrix}, \begin{bmatrix} \frac{1}{\sqrt{2}} \mathbf{u}_m \\ -\frac{1}{\sqrt{2}} \mathbf{v}_m \end{bmatrix}, \dots, \begin{bmatrix} \frac{1}{\sqrt{2}} \mathbf{u}_2 \\ -\frac{1}{\sqrt{2}} \mathbf{v}_2 \end{bmatrix}, \begin{bmatrix} \frac{1}{\sqrt{2m}} \mathbf{1}_m \\ -\frac{1}{\sqrt{2n}} \mathbf{1}_n \end{bmatrix} \right\},
\end{aligned} \tag{43}$$

are eigenvectors of L with eigenvalues $\{\lambda_1, \dots, \lambda_{m+n}\} = \{0, 1 - s_2, \dots, 1 - s_m, 1, \dots, 1, 1 + s_m, \dots, 1 + s_2, 2\}$, where $\{\mathbf{v}_{m+1}, \dots, \mathbf{v}_{m+n}\} \subset \mathbb{R}^n$ is any set of orthonormal vectors that are orthogonal to $\{\mathbf{v}_1, \dots, \mathbf{v}_m\}$. To

prove the quadratic form, we write

$$\begin{aligned}
& \frac{1}{\sqrt{mn}} \sum_{ij} (\sqrt{m}\mathbf{g}[i] - \sqrt{n}\mathbf{h}[j])^2 W_{i,j} \\
&= \sqrt{\frac{m}{n}} \sum_i (\mathbf{g}[i])^2 \sum_j W_{i,j} + \sqrt{\frac{n}{m}} \sum_j (\mathbf{h}[j])^2 \sum_i W_{i,j} - 2 \sum_{ij} \mathbf{g}[i] W_{i,j} \mathbf{h}[j] \\
&= \|\mathbf{g}\|_2^2 + \|\mathbf{h}\|_2^2 - 2\mathbf{g}^T W \mathbf{h} = \|\mathbf{f}\|_2^2 - \mathbf{f}^T \hat{W} \mathbf{f} = \mathbf{f}^T L \mathbf{f}, \tag{44}
\end{aligned}$$

where we used the fact that $W \in \mathcal{B}_{m,n}$ (see (2)). For the second part of Proposition 2, the facts that \tilde{L} shares the eigenvalues of L and $\psi_k = D\phi_k/\|D\phi_k\|_2$ follow from the similarity of $\tilde{L} = DLD^{-1}$ to L . Therefore, eq. (10) follows immediately from (43) and the embedding formula (5).

Appendix C Proof of Proposition 3

For even t , we have

$$\begin{aligned}
D_{\mathcal{X}}^{(t)}(\mathbf{x}_i, \mathbf{x}_{i'}) &= \sqrt{m} \left\| \left[P_{\mathcal{X}\mathcal{X}}^{(t)} \right]_{i,\cdot} - \left[P_{\mathcal{X}\mathcal{X}}^{(t)} \right]_{i',\cdot} \right\|_2 = \sqrt{m} \left\| \sum_{k=1}^m \mathbf{u}_k[i] s_k \mathbf{u}_k^T - \sum_{k=1}^m \mathbf{u}_k[i'] s_k \mathbf{u}_k^T \right\|_2 \\
&= \sqrt{\sum_{k=1}^m s_k^{2t} (\sqrt{m}\mathbf{u}_k[i] - \sqrt{m}\mathbf{u}_k[i'])^2} = \sqrt{\sum_{k=2}^m s_k^{2t} (\sqrt{m}\mathbf{u}_k[i] - \sqrt{m}\mathbf{u}_k[i'])^2} = \|\tilde{x}_i - \tilde{x}_{i'}\|_2, \tag{45}
\end{aligned}$$

$$\begin{aligned}
D_{\mathcal{Y}}^{(t)}(\mathbf{y}_j, \mathbf{y}_{j'}) &= \sqrt{n} \left\| \left[P_{\mathcal{Y}\mathcal{Y}}^{(t)} \right]_{j,\cdot} - \left[P_{\mathcal{Y}\mathcal{Y}}^{(t)} \right]_{j',\cdot} \right\|_2 = \sqrt{n} \left\| \sum_{k=1}^m \mathbf{v}_k[j] s_k \mathbf{v}_k^T - \sum_{k=1}^m \mathbf{v}_k[j'] s_k \mathbf{v}_k^T \right\|_2 \\
&= \sqrt{\sum_{k=1}^m s_k^{2t} (\sqrt{n}\mathbf{v}_k[j] - \sqrt{n}\mathbf{v}_k[j'])^2} = \sqrt{\sum_{k=2}^m s_k^{2t} (\sqrt{n}\mathbf{v}_k[j] - \sqrt{n}\mathbf{v}_k[j'])^2} = \|\tilde{y}_j - \tilde{y}_{j'}\|_2, \tag{46}
\end{aligned}$$

where we used the fact that $\mathbf{u}_1 = \mathbf{1}_m/\sqrt{m}$ and $\mathbf{v}_1 = \mathbf{1}_n/\sqrt{n}$. Similarly, for odd t ,

$$\begin{aligned}
D_{\mathcal{X}}^{(t)}(\mathbf{x}_i, \mathbf{x}_{i'}) &= \sqrt{n} \left\| \left[P_{\mathcal{X}\mathcal{Y}}^{(t)} \right]_{i,\cdot} - \left[P_{\mathcal{X}\mathcal{Y}}^{(t)} \right]_{i',\cdot} \right\|_2 = \sqrt{n} \left\| \sqrt{\frac{m}{n}} \sum_{k=1}^m \mathbf{u}_k[i] s_k \mathbf{v}_k^T - \sqrt{\frac{m}{n}} \sum_{k=1}^m \mathbf{u}_k[i'] s_k \mathbf{v}_k^T \right\|_2 \\
&= \sqrt{\sum_{k=1}^m s_k^{2t} (\sqrt{m}\mathbf{u}_k[i] - \sqrt{m}\mathbf{u}_k[i'])^2} = \sqrt{\sum_{k=2}^m s_k^{2t} (\sqrt{m}\mathbf{u}_k[i] - \sqrt{m}\mathbf{u}_k[i'])^2} = \|\tilde{x}_i - \tilde{x}_{i'}\|_2, \tag{47}
\end{aligned}$$

$$\begin{aligned}
D_{\mathcal{Y}}^{(t)}(\mathbf{y}_j, \mathbf{y}_{j'}) &= \sqrt{m} \left\| \left[P_{\mathcal{Y}\mathcal{X}}^{(t)} \right]_{j,\cdot} - \left[P_{\mathcal{Y}\mathcal{X}}^{(t)} \right]_{j',\cdot} \right\|_2 = \sqrt{m} \left\| \sqrt{\frac{n}{m}} \sum_{k=1}^m \mathbf{v}_k[j] s_k \mathbf{u}_k^T - \sqrt{\frac{n}{m}} \sum_{k=1}^m \mathbf{v}_k[j'] s_k \mathbf{u}_k^T \right\|_2 \\
&= \sqrt{\sum_{k=1}^m s_k^{2t} (\sqrt{n}\mathbf{v}_k[j] - \sqrt{n}\mathbf{v}_k[j'])^2} = \sqrt{\sum_{k=2}^m s_k^{2t} (\sqrt{n}\mathbf{v}_k[j] - \sqrt{n}\mathbf{v}_k[j'])^2} = \|\tilde{y}_j - \tilde{y}_{j'}\|_2. \tag{48}
\end{aligned}$$

Lastly, we have

$$\begin{aligned} D_{\mathcal{X}\mathcal{Y}}^{(t)}(x_i, y_j) &= \sqrt{m} \left\| \left[P_{\mathcal{X}\mathcal{X}}^{(t)} \right]_{i,\cdot} - \left[P_{\mathcal{Y}\mathcal{X}}^{(t)} \right]_{j,\cdot} \right\|_2 = \sqrt{m} \left\| \sum_{k=1}^m \mathbf{u}_k[i] s_k \mathbf{u}_k^T - \sqrt{\frac{n}{m}} \sum_{k=1}^m \mathbf{v}_k[j] s_k \mathbf{u}_k^T \right\|_2 \\ &= \sqrt{\sum_{k=1}^m s_k^{2t} (\sqrt{m} \mathbf{u}_k[i] - \sqrt{n} \mathbf{v}_k[j])^2} = \sqrt{\sum_{k=2}^m s_k^{2t} (\sqrt{m} \mathbf{u}_k[i] - \sqrt{n} \mathbf{v}_k[j])^2} = \|\tilde{x}_i - \tilde{y}_j\|_2, \end{aligned} \quad (49)$$

$$\begin{aligned} D_{\mathcal{Y}\mathcal{X}}^{(t)}(y_j, x_i) &= \sqrt{n} \left\| \left[P_{\mathcal{Y}\mathcal{Y}}^{(t)} \right]_{j,\cdot} - \left[P_{\mathcal{X}\mathcal{Y}}^{(t)} \right]_{i,\cdot} \right\|_2 = \sqrt{n} \left\| \sum_{k=1}^m \mathbf{v}_k[j] s_k \mathbf{v}_k^T - \sqrt{\frac{m}{n}} \sum_{k=1}^m \mathbf{u}_k[i] s_k \mathbf{v}_k^T \right\|_2 \\ &= \sqrt{\sum_{k=1}^m s_k^{2t} (\sqrt{m} \mathbf{u}_k[i] - \sqrt{n} \mathbf{v}_k[j])^2} = \sqrt{\sum_{k=2}^m s_k^{2t} (\sqrt{m} \mathbf{u}_k[i] - \sqrt{n} \mathbf{v}_k[j])^2} = \|\tilde{x}_i - \tilde{y}_j\|_2, \end{aligned} \quad (50)$$

which concludes the proof.

Appendix D Supporting lemmas and definitions for Theorem 4

D.1 Matrix scaling

We now provide some basic results on the stability of matrix scaling [57, 58], namely, the process of diagonally scaling a positive matrix $A \in \mathbb{R}^{m \times n}$ to have certain prescribed row and column sums. The definitions and results below are adapted from [32]. Let $\alpha = [\alpha_1, \dots, \alpha_m]$, $\beta = [\beta_1, \dots, \beta_n]$, $\mathbf{r} = [r_1, \dots, r_m]$, and $\mathbf{c} = [c_1, \dots, c_n]$ be (entrywise) positive vectors with $\|\mathbf{r}\|_1 = \|\mathbf{c}\|_1$, and denote $B = \text{diag}\{\alpha\} A \text{diag}\{\beta\}$, where $\text{diag}\{\alpha\}$ denotes a diagonal matrix with α on its main diagonal. We say that the pair of vectors (α, β) *scales* A to row sums \mathbf{r} and column sums \mathbf{c} , if

$$r_i = \sum_{j=1}^n B_{i,j} = \sum_{j=1}^n \alpha_i A_{i,j} \beta_j, \quad \text{and} \quad c_j = \sum_{i=1}^m B_{i,j} = \sum_{i=1}^m \alpha_i A_{i,j} \beta_j, \quad (51)$$

for all $i \in [m]$ and $j \in [n]$. We refer to α and β from (51) (or their entries) as *scaling factors* of A . Let us define

$$\bar{r}_i = \frac{r_i}{\sqrt{s}}, \quad \bar{c}_j = \frac{c_j}{\sqrt{s}}, \quad s = \|\mathbf{r}\|_1 = \|\mathbf{c}\|_1, \quad (52)$$

for $i \in [m]$ and $j \in [n]$. The following lemma describes a useful normalization of the scaling factors and the resulting bounds on their entries; see [32].

Lemma 7 (Boundedness of scaling factors [32]). *Let $A \in \mathbb{R}^{m \times n}$ be a matrix with positive entries and denote $a = \min_{i,j} A_{i,j}$ and $b = \max_{i,j} A_{i,j}$. Then, there exists a unique pair of positive vectors (α, β) with $\|\alpha\|_1 = \|\beta\|_1$ that scales A to row sums \mathbf{r} and column sums \mathbf{c} . Moreover, for all $i \in [m]$ and $j \in [n]$, we have*

$$\frac{\sqrt{a}}{b} \leq \frac{\alpha_i}{\bar{r}_i} \leq \frac{\sqrt{b}}{a}, \quad \frac{\sqrt{a}}{b} \leq \frac{\beta_j}{\bar{c}_j} \leq \frac{\sqrt{b}}{a}. \quad (53)$$

The following lemma characterizes the stability of the scaling factors to perturbations in the row and column sums. In particular, it states that if there exists a pair of positive vectors $(\hat{\alpha}, \hat{\beta})$ that approximately scales A to certain row and column sums, then $(\hat{\alpha}, \hat{\beta})$ must be close to a true pair of scaling factors for these row and column sums.

Lemma 8 (Stability of scaling factors under approximate scaling). *Let $A \in \mathbb{R}^{m \times n}$ be a matrix with positive entries and denote $a = \min_{i,j} A_{i,j}$, $b = \max_{i,j} A_{i,j}$. Suppose that there exists $\epsilon \in (0, 1)$ and positive vectors $\hat{\alpha} = [\hat{\alpha}_1, \dots, \hat{\alpha}_m]$ and $\hat{\beta} = [\hat{\beta}_1, \dots, \hat{\beta}_n]$, such that*

$$\left| \frac{1}{c_j} \sum_{i=1}^m \hat{\alpha}_i A_{i,j} \hat{\beta}_j - 1 \right| \leq \epsilon, \quad \left| \frac{1}{r_i} \sum_{j=1}^n \hat{\alpha}_i A_{i,j} \hat{\beta}_j - 1 \right| \leq \epsilon, \quad (54)$$

for all $i \in [m]$ and $j \in [n]$. Then, there exists a pair of positive vectors (α, β) that scales A to row sums \mathbf{r} and column sums \mathbf{c} , satisfying

$$\frac{|\alpha_i - \hat{\alpha}_i|}{\hat{\alpha}_i} \leq \epsilon \left(\frac{1}{1 - \epsilon} + \frac{4s\sqrt{b}}{a^2 C_1^{3/2} C_2^{3/2} m \min_i r_i} \right), \quad (55)$$

$$\frac{|\beta_j - \hat{\beta}_j|}{\hat{\beta}_j} \leq \epsilon \left(\frac{1}{1 - \epsilon} + \frac{4s\sqrt{b}}{a^2 C_1^{3/2} C_2^{3/2} n \min_j c_j} \right), \quad (56)$$

for all $i \in [m]$ and $j \in [n]$, where $C_1 = \min_i \{\hat{\alpha}_i / \bar{r}_i\}$ and $C_2 = \min_j \{\hat{\beta}_j / \bar{c}_j\}$.

An argument very similar to Lemma 8 is outlined inside the proof of Theorem 2 in [32] in a more specialized setting. For completeness, we provide the full proof of Lemma 8 below.

Proof. Let $(\tilde{\alpha}, \tilde{\beta})$ be the unique pair of scaling factors of A with $\|\tilde{\alpha}\|_1 = \|\tilde{\beta}\|_1$ (see Lemma 7), and define

$$B_{i,j} = \hat{\alpha}_i A_{i,j} \hat{\beta}_j, \quad \tilde{B}_{i,j} = \tilde{\alpha}_i A_{i,j} \tilde{\beta}_j = u_i B_{i,j} v_j, \quad u_i = \frac{\tilde{\alpha}_i}{\hat{\alpha}_i}, \quad v_j = \frac{\tilde{\beta}_j}{\hat{\beta}_j}, \quad (57)$$

for all $i \in [m]$ and $j \in [n]$. Observe that $\sum_i \tilde{B}_{i,j} = c_j$, $\sum_j \tilde{B}_{i,j} = r_i$, and

$$\left| \frac{1}{c_j} \sum_{i=1}^m B_{i,j} - 1 \right| \leq \epsilon, \quad \left| \frac{1}{r_i} \sum_{j=1}^n B_{i,j} - 1 \right| \leq \epsilon, \quad (58)$$

for all $i \in [m]$, $j \in [n]$. Using the first inequality in (58) for $j = \operatorname{argmin}_k v_k$, we have

$$1 = \frac{1}{c_j} \sum_{i=1}^m \tilde{B}_{i,j} = \frac{1}{c_j} \sum_{i=1}^m u_i B_{i,j} v_j \leq \min_j v_j \max_i u_i \frac{1}{c_j} \sum_{i=1}^m B_{i,j} \leq (1 + \epsilon) \min_j v_j \max_i u_i. \quad (59)$$

Similarly, using the second inequality in (58) for $i = \operatorname{argmax}_\ell v_\ell$ gives

$$1 = \frac{1}{r_i} \sum_{j=1}^n \tilde{B}_{i,j} = \frac{1}{r_i} \sum_{j=1}^n u_i B_{i,j} v_j \geq \max_i u_i \min_j v_j \frac{1}{r_i} \sum_{j=1}^n B_{i,j} \geq (1 - \epsilon) \max_i u_i \min_j v_j, \quad (60)$$

and by combining (59) and (60) we obtain

$$\frac{1}{1 + \epsilon} \leq \max_i u_i \min_j v_j \leq \frac{1}{1 - \epsilon}. \quad (61)$$

Analogously to (59) and (60), it is easy to verify that by using the first inequality in (58) for $j = \operatorname{argmax}_k v_k$ and using the second inequality in (58) for $i = \operatorname{argmin}_\ell v_\ell$, one gets

$$\frac{1}{1 + \epsilon} \leq \min_i u_i \max_j v_j \leq \frac{1}{1 - \epsilon}. \quad (62)$$

Note that (62) can also be obtained directly from (61) by a symmetry argument, that is, by considering (61) in the setting when A is replaced with its transpose, thereby interchanging the roles of \mathbf{u} and \mathbf{v} . In addition, according to Lemma 7 and using the fact that $\hat{\alpha}_i \geq C_1 \bar{r}_i$ and $\hat{\beta}_j \geq C_2 \bar{c}_j$ (from the definition of C_1 and C_2 in Lemma 8), it follows that for all $i \in [m]$ and $j \in [n]$

$$u_i \leq \frac{\sqrt{b}}{aC_1}, \quad v_j \leq \frac{\sqrt{b}}{aC_2}. \quad (63)$$

Let us denote $\ell = \operatorname{argmax}_i u_i$. By the second inequality in (58) together with (61), we can write

$$1 = \frac{1}{r_\ell} \sum_{j=1}^n \tilde{B}_{\ell,j} = \frac{1}{r_\ell} \sum_{j=1}^n u_\ell B_{\ell,j} v_j \geq \frac{1}{(1 + \epsilon)r_\ell} \sum_{j=1}^n B_{\ell,j} \frac{v_j}{\min_j v_j}, \quad (64)$$

implying that

$$\frac{1}{r_\ell} \sum_{j=1}^n B_{\ell,j} \left(\frac{v_j}{\min_j v_j} - 1 \right) \leq 1 + \epsilon - \frac{1}{r_\ell} \sum_{j=1}^n B_{\ell,j} \leq 2\epsilon. \quad (65)$$

Multiplying (65) by $\min_j v_j / \min_j B_{\ell,j}$, it follows that

$$\frac{1}{r_\ell} \sum_{j=1}^n (v_j - \min_j v_j) \leq \frac{1}{r_\ell} \sum_{j=1}^n \frac{B_{\ell,j}}{\min_j B_{\ell,j}} (v_j - \min_j v_j) \leq 2\epsilon \frac{\min_j v_j}{\min_j B_{\ell,j}} \leq \frac{2\epsilon \min_j v_j}{aC_1 C_2 \bar{r}_\ell \min_j \bar{c}_j}, \quad (66)$$

where we used the definition of B together with the conditions in Lemma 8. Multiplying (66) by r_ℓ/n and employing the definitions of \bar{r}_i and \bar{c}_j (see (52)) gives

$$\frac{1}{n} \sum_{j=1}^n (v_j - \min_j v_j) \leq \frac{2\epsilon s \min_j v_j}{aC_1 C_2 n \min_j c_j} \leq \frac{2\epsilon s \max_j v_j}{aC_1 C_2 n \min_j c_j}. \quad (67)$$

We next provide a derivation analogous to (64)–(67) to obtain a bound for $\frac{1}{n} \sum_{j=1}^n (\max_j v_j - v_j)$. Let us denote $t = \operatorname{argmin}_i u_i$. Using the second inequality in (58) together with (62), we have

$$1 = \frac{1}{r_t} \sum_{j=1}^n \tilde{B}_{t,j} = \frac{1}{r_t} \sum_{j=1}^n u_t B_{t,j} v_j \leq \frac{1}{(1-\epsilon)r_t} \sum_{j=1}^n B_{t,j} \frac{v_j}{\max_j v_j}, \quad (68)$$

and therefore

$$\frac{1}{r_t} \sum_{j=1}^n B_{t,j} \left(1 - \frac{v_j}{\max_j v_j} \right) \leq \frac{1}{r_t} \sum_{j=1}^n B_{t,j} - (1-\epsilon) \leq 2\epsilon. \quad (69)$$

Multiplying the above by $\max_j v_j / \min_j B_{t,j}$, it follows that

$$\frac{1}{r_t} \sum_{j=1}^n (\max_j v_j - v_j) \leq \frac{1}{r_t} \sum_{j=1}^n \frac{B_{t,j}}{\min_j B_{t,j}} (\max_j v_j - v_j) \leq 2\epsilon \frac{\max_j v_j}{\min_j B_{t,j}} \leq \frac{2\epsilon \max_j v_j}{aC_1 C_2 \bar{r}_t \min_j \bar{c}_j}. \quad (70)$$

Furthermore, multiplying the above by r_t/n and using the definitions of \bar{r}_i and \bar{c}_j (see (52)), we get

$$\frac{1}{n} \sum_{j=1}^n (\max_j v_j - v_j) \leq 2\epsilon \frac{\max_j v_j}{\min_j B_{t,j}} \leq \frac{2\epsilon s \max_j v_j}{aC_1 C_2 n \min_j c_j}. \quad (71)$$

Lastly, summing (67) and (71) gives

$$\max_j v_j - \min_j v_j \leq \frac{4\epsilon s \max_j v_j}{aC_1 C_2 n \min_j c_j}. \quad (72)$$

It is easy to verify that by repeating the derivation of (64) – (72) analogously for u_i instead of v_j , we get

$$\max_i u_i - \min_i u_i \leq \frac{4\epsilon s \max_i u_i}{aC_1 C_2 m \min_i r_i}. \quad (73)$$

We omit the full derivation for the sake of brevity. Note that (73) can also be obtained directly from (72) by a symmetry argument, namely by considering (72) in the setting where A is replaced with its transpose, so that n is replaced with m , \mathbf{c} is replaced with \mathbf{r} , and \mathbf{v} is replaced with \mathbf{u} .

Observe that $|\tau - v_j| \leq \max_j v_j - \min_j v_j$ for any $\tau \in [\min_j v_j, \max_j v_j]$ and all $j \in [n]$. Taking τ as the geometric mean of $\max_j v_j$ and $\min_j v_j$, together with (72) gives

$$\left| \sqrt{\max_j v_j \min_j v_j} - v_j \right| \leq \frac{4\epsilon s \max_j v_j}{aC_1 C_2 n \min_j c_j}, \quad (74)$$

for all $j \in [n]$. Multiplying both hand sides of (74) by $\gamma^{-1} = \sqrt{\max_i u_i / \max_j v_j}$ we get

$$\left| \sqrt{\max_i u_i \min_j v_j} - \gamma^{-1} v_j \right| \leq \frac{4\epsilon s \sqrt{\max_j v_j \max_i u_i}}{a C_1 C_2 n \min_j c_j} \leq \frac{4\epsilon s \sqrt{b}}{a^2 C_1^{3/2} C_2^{3/2} n \min_j c_j}, \quad (75)$$

where we also used (63) in the last inequality. According to (61), we have for all $\epsilon \in (0, 1)$ that

$$1 - \frac{\epsilon}{1 - \epsilon} \leq \frac{1}{1 + \epsilon} \leq \sqrt{\frac{1}{1 + \epsilon}} \leq \sqrt{\max_i u_i \min_j v_j} \leq \sqrt{\frac{1}{1 - \epsilon}} \leq \frac{1}{1 - \epsilon} = 1 + \frac{\epsilon}{1 - \epsilon}, \quad (76)$$

which together with (74) implies that

$$|1 - \gamma^{-1} v_j| \leq \frac{\epsilon}{1 - \epsilon} + \frac{4\epsilon s \sqrt{b}}{a^2 C_1^{3/2} C_2^{3/2} n \min_j c_j}. \quad (77)$$

Analogously to (74), from (73) we obtain

$$\left| \sqrt{\max_i u_i \min_i u_i} - u_i \right| \leq \frac{4\epsilon s \max_i u_i}{a C_1 C_2 m \min_i r_i}, \quad (78)$$

for all $i \in [m]$. Multiplying both hand sides of (78) by $\gamma = \sqrt{\max_j v_j / \max_i u_i}$ we get

$$\left| \sqrt{\max_j v_j \min_i u_i} - \gamma u_i \right| \leq \frac{4\epsilon s \sqrt{\max_j v_j \max_i u_i}}{a C_1 C_2 m \min_i r_i} \leq \frac{4\epsilon s \sqrt{b}}{a^2 C_1^{3/2} C_2^{3/2} m \min_i r_i}. \quad (79)$$

Consequently, using (62), and analogously to the derivation of (77), it follows that

$$|1 - \gamma u_i| \leq \frac{\epsilon}{1 - \epsilon} + \frac{4\epsilon s \sqrt{b}}{a^2 C_1^{3/2} C_2^{3/2} m \min_i r_i}, \quad (80)$$

which together with the definition of \mathbf{u} and \mathbf{v} in (57) concludes the proof, taking $\alpha = \gamma \tilde{\alpha}$ and $\beta = \gamma^{-1} \tilde{\beta}$. \square

D.2 Concentration of inner products in the latent manifold model

The following lemma characterizes the concentration of the inner products $\langle x_i - \nu_1, y_j - \nu_2 \rangle$ with respect to the quantities in the latent manifold model (24).

Lemma 9. *Under Assumption 1, there exist universal constants $c, p_0, \tau_0 > 0$, such that for any $i \in [m]$ and $j \in [n]$, and for all $\tau > \tau_0$ and $p > p_0$, we have*

$$\Pr \left\{ \left| \langle x_i - \nu_1, y_j - \nu_2 \rangle - a_1 a_2 \langle \bar{x}_i, \bar{y}_j \rangle \right| > c \tau \sqrt{\log p} \cdot \max\{E, E^2 \sqrt{p}\} \right\} \leq p^{-\tau}. \quad (81)$$

The proof (provided below) is very similar to the proof of Lemma SM1.1 in [33], adapted here to support the latent manifold model (24).

Proof. According to the latent manifold model (24), we can write

$$\langle x_i - \nu_1, y_j - \nu_2 \rangle = a_1 a_2 \langle \bar{x}_i, \bar{y}_j \rangle + \langle \eta_i^{(1)}, h_j^{(1)} \rangle + \langle \eta_j^{(2)}, h_i^{(1)} \rangle + \langle \eta_i^{(1)}, \eta_j^{(2)} \rangle, \quad (82)$$

where we defined

$$h_i^{(1)} = a_1 \mathcal{U} \bar{x}_i + \mathcal{V}_1 z_i^{(1)}, \quad h_j^{(2)} = a_2 \mathcal{U} \bar{y}_j + \mathcal{V}_2 z_j^{(2)}, \quad (83)$$

for $i = 1, \dots, m$ and $j = 1, \dots, n$. Conditioning on $h_j^{(2)}$, the random variable $\langle \eta_i^{(1)}, h_j^{(2)} \rangle$ is sub-Gaussian for each $i = 1, \dots, m$, satisfying

$$\|\langle \eta_i^{(1)}, h_j^{(2)} \rangle\|_{\psi_2} \leq \|h_j^{(2)}\|_2 \sup_{\|y\|_2=1} \|\langle \eta_i^{(1)}, y \rangle\|_{\psi_2} \leq C(C+1)E, \quad (84)$$

where we used the definition of the sub-Gaussian norm [65] and the fact that

$$\|h_j^{(2)}\|_2 \leq a_1 \|\bar{x}_i\|_2 + \|z_i^{(1)}\|_2 \leq C(C+1), \quad (85)$$

according to Assumption 1. Therefore, according to Proposition 2.5.2 in [65], we have

$$\Pr \left\{ \left| \langle \eta_i^{(1)}, h_j^{(2)} \rangle \right| > \tau \right\} \leq 2 \exp \left\{ -\frac{\tau^2}{\tilde{c}^2 \|\langle \eta_i^{(1)}, h_j^{(2)} \rangle\|_{\psi_2}^2} \right\} \leq 2 \exp \left\{ -\frac{\tau^2}{\tilde{c}^2 C^2 (C+1)^2 E^2} \right\}, \quad (86)$$

for a universal constant $\tilde{c} > 0$. Taking $\tau = \tilde{c}C(C+1)E\sqrt{t \log p}$, for any $t > 0$, shows that

$$\Pr \left\{ \left| \langle \eta_i^{(1)}, h_j^{(2)} \rangle \right| > \tilde{c}C(C+1)E\sqrt{t \log p} \right\} \leq 2p^{-t}. \quad (87)$$

Since (87) holds conditionally on any realization of $h_j^{(2)}$, it also holds unconditionally. Analogously to the derivation of the probabilistic bound (87), it can be verified that

$$\Pr \left\{ \left| \langle \eta_j^{(2)}, h_i^{(1)} \rangle \right| > \tilde{c}C(C+1)E\sqrt{t \log p} \right\} \leq 2p^{-t}. \quad (88)$$

For the last term in (82), we have that

$$\Pr \left\{ \left| \langle \eta_i^{(1)}, \eta_j^{(2)} \rangle \right| > E^2 \left(\tilde{c}_1 \sqrt{tp \log p} + \tilde{c}_2 t \log p \right) \right\} \leq 3p^{-t}, \quad (89)$$

for all $t > 0$, where $\tilde{c}_1, \tilde{c}_2 > 0$ are universal constants; see the proof of Lemma SM1.1 in [33] and specifically the probabilistic bound on $\langle \eta_i, \eta_j \rangle$ in eq. SM1.11 therein. Overall, combining (89), (87), (88), and (82), applying the union bound, absorbing any constants multiplying p^{-t} into the constant c in (81), and replacing t with τ , provides the required result. \square

D.3 Order with high probability in n

For brevity of our proofs, we will use the following definition.

Definition 10 (Order with high probability in n). Let X be a real-valued random variable that may depend on ε , m , n , and p , and suppose that $f(m, n, p)$ is a real-valued function of m, n, p . We say that $X = \mathcal{O}_n^{(\varepsilon)}(f(m, n, p))$ if there exist global constants $\tau_0, n_0(\varepsilon), C'(\varepsilon) > 0$, such that for all $n \geq n_0(\varepsilon)$, $m \geq n^\gamma$, and $p \geq n^\gamma$ (where γ is from Assumption 2), we have

$$|X| \leq \tau C'(\varepsilon) f(m, n, p), \quad (90)$$

with probability at least $1 - n^{-\tau}$, for all $\tau \geq \tau_0$.

Definition 10 is convenient for our subsequent analysis. First, if we have a collection of random variables $X_1, \dots, X_{P(n)}$, where $X_i = \mathcal{O}_{m,n,p}^{(\varepsilon)}(f(m, n, p))$ for $i = 1, \dots, P(n)$ and $P(n)$ is a fixed polynomial in n whose coefficients are global constants, then we immediately get (by applying the union bound $P(n)$ times)

$$\max_{i=1, \dots, P(n)} |X_i| = \mathcal{O}_n^{(\varepsilon)}(f(m, n, p)). \quad (91)$$

Second, if $X = \mathcal{O}_n^{(\varepsilon)}(f(m, n, p))$ and $Y = g^{(\varepsilon)}(X)$, where $g^{(\varepsilon)} \in \mathcal{C}^1(\mathbb{R})$ for all $\varepsilon > 0$ and $\lim_{m,n,p \rightarrow \infty} f(m, n, p) = 0$, then by a Taylor expansion of $g^{(\varepsilon)}(x)$ around zero,

$$Y = g^{(\varepsilon)}(0) + \mathcal{O}_n^{(\varepsilon)}(f(m, n, p)). \quad (92)$$

We will use properties (91) and (92) of Definition 10 seamlessly throughout the remaining proofs.

Appendix E Proof of Theorem 4

Let us write

$$\begin{aligned} K_{i,j} &= \exp \left\{ -\frac{\|x_i - y_j\|_2^2}{\varepsilon} \right\} = \exp \left\{ -\frac{\|x_i\|_2^2}{\varepsilon} \right\} \exp \left\{ \frac{2\langle x_i, y_j \rangle}{\varepsilon} \right\} \exp \left\{ -\frac{\|y_j\|_2^2}{\varepsilon} \right\} \\ &= \exp \left\{ \frac{-\|x_i\|_2^2 + \langle 2x_i - \nu_1, \nu_2 \rangle}{\varepsilon} \right\} \exp \left\{ \frac{2\langle x_i - \nu_1, y_j - \nu_2 \rangle}{\varepsilon} \right\} \exp \left\{ \frac{-\|y_j\|_2^2 + \langle \nu_1, 2y_j - \nu_2 \rangle}{\varepsilon} \right\}. \end{aligned} \quad (93)$$

Therefore, we have

$$W_{i,j} = \alpha_i K_{i,j} \beta_j = \tilde{\alpha}_i \tilde{K}_{i,j} \tilde{\beta}_j, \quad (94)$$

where we defined

$$\tilde{\alpha}_i = \alpha_i \exp \left\{ \frac{-\|x_i\|_2^2 + \langle 2x_i - \nu_1, \nu_2 \rangle}{\varepsilon} \right\}, \quad (95)$$

$$\tilde{\beta}_j = \beta_j \exp \left\{ \frac{-\|y_j\|_2^2 + \langle 2y_j - \nu_2, \nu_1 \rangle}{\varepsilon} \right\}, \quad (96)$$

$$\tilde{K}_{i,j} = \exp \left\{ \frac{2\langle x_i - \nu_1, y_j - \nu_2 \rangle}{\varepsilon} \right\}. \quad (97)$$

According to Lemma 9, Assumptions 1 and 2, and Definition 10, we have

$$\begin{aligned} \tilde{K}_{i,j} &= \exp \left\{ \frac{2a_1 a_2 \langle \bar{x}_i, \bar{y}_j \rangle + \mathcal{O}_n^{(\varepsilon)} \left(\max \{ E\sqrt{\log p}, E^2\sqrt{p \log p} \} \right)}{\varepsilon} \right\} \\ &= \exp \left\{ \frac{2a_1 a_2 \langle \bar{x}_i, \bar{y}_j \rangle}{\varepsilon} \right\} \exp \left\{ \frac{\mathcal{O}_n^{(\varepsilon)} \left(\max \{ E\sqrt{\log p}, E^2\sqrt{p \log p} \} \right)}{\varepsilon} \right\} \end{aligned} \quad (98)$$

$$= \exp \left\{ \frac{2\langle \bar{x}_i, \bar{y}_j \rangle}{\varepsilon/(a_1 a_2)} \right\} \left[1 + \mathcal{O}_n^{(\varepsilon)} \left(\max \{ E\sqrt{\log p}, E^2\sqrt{p \log p} \} \right) \right], \quad (99)$$

for all $i \in [m]$ and $j \in [n]$, where we used the two properties of Definition 10 mentioned in Section D.3 (noting that $\max \{ E\sqrt{\log p}, E^2\sqrt{p \log p} \} \rightarrow 0$ as $n \rightarrow \infty$ due to Assumptions 1 and 2).

Let us define

$$\hat{\varepsilon} = \frac{\varepsilon}{a_1 a_2}, \quad \hat{\alpha}_i = \frac{1}{(\pi \hat{\varepsilon})^{d/4} \sqrt{m}} \rho_{\hat{\varepsilon}}(\bar{x}_i) \exp \left\{ -\frac{\|\bar{x}_i\|_2^2}{\hat{\varepsilon}} \right\}, \quad \hat{\beta}_j = \frac{1}{(\pi \hat{\varepsilon})^{d/4} \sqrt{n}} \rho_{\hat{\varepsilon}}(\bar{y}_j) \exp \left\{ -\frac{\|\bar{y}_j\|_2^2}{\hat{\varepsilon}} \right\}, \quad (100)$$

for all $i \in [m]$ and $j \in [n]$. According to (94) and our definition of $\mathcal{B}_{m,n}$ from (2), the matrix \tilde{K} is scaled to prescribed row sums $r_i = \sqrt{n/m}$ and column sums $c_j = \sqrt{m/n}$ (see definitions and notation in Section D.1) by the pair of scaling factors $(\tilde{\alpha}, \tilde{\beta})$. We now proceed to show that \tilde{K} is also approximately scaled to the same prescribed row and column sums by the pair $(\hat{\alpha}, \hat{\beta})$. We have

$$\begin{aligned} \frac{1}{c_j} \sum_{i=1}^m \hat{\alpha}_i \tilde{K}_{i,j} \hat{\beta}_j &= \frac{1}{(\pi \hat{\varepsilon})^{d/2} m} \sum_{i=1}^m \rho_{\hat{\varepsilon}}(\bar{x}_i) \exp \left\{ \frac{\|\bar{x}_i - \bar{y}_j\|_2^2}{\hat{\varepsilon}} \right\} \rho_{\hat{\varepsilon}}(\bar{y}_j) \left[1 + \mathcal{O}_n^{(\varepsilon)} \left(\max \{ E\sqrt{\log p}, E^2\sqrt{p \log p} \} \right) \right] \\ &= \frac{1}{(\pi \hat{\varepsilon})^{d/2} m} \sum_{i=1}^m \rho_{\hat{\varepsilon}}(\bar{x}_i) \exp \left\{ \frac{\|\bar{x}_i - \bar{y}_j\|_2^2}{\hat{\varepsilon}} \right\} \rho_{\hat{\varepsilon}}(\bar{y}_j) + \mathcal{O}_n^{(\varepsilon)} \left(\max \{ E\sqrt{\log p}, E^2\sqrt{p \log p} \} \right), \end{aligned} \quad (101)$$

for all $j \in [n]$, where we used Assumption 1 and the fact that $\rho_{\hat{\varepsilon}}$ is bounded (see the text after (26)) in the last transition. Conditioning on \bar{y}_j , we apply Hoeffding's inequality and utilize Assumption 2, obtaining

$$\begin{aligned} \frac{1}{c_j} \sum_{i=1}^m \hat{\alpha}_i \tilde{K}_{i,j} \hat{\beta}_j &= \int_{\mathcal{M}} \rho_{\hat{\varepsilon}}(x) \mathcal{K}_{\hat{\varepsilon}}(x, \bar{y}_j) \rho_{\hat{\varepsilon}}(\bar{y}_j) \omega(x) d\mu(x) + \mathcal{O}_n^{(\varepsilon)} \left(\sqrt{\frac{\log m}{m}} \right) + \mathcal{O}_n^{(\varepsilon)} \left(\max \{ E\sqrt{\log p}, E^2\sqrt{p \log p} \} \right) \\ &= 1 + \mathcal{O}_n^{(\varepsilon)} \left(\max \left\{ E\sqrt{\log p}, E^2\sqrt{p \log p}, \sqrt{\frac{\log m}{m}} \right\} \right), \end{aligned} \quad (102)$$

for all $i \in [m]$, where we also used (26). Similarly, we have

$$\begin{aligned}
\frac{1}{r_i} \sum_{j=1}^n \hat{\alpha}_i \tilde{K}_{i,j} \hat{\beta}_j &= \frac{1}{(\pi \hat{\varepsilon})^{d/2} n} \sum_{j=1}^n \rho_{\hat{\varepsilon}}(\bar{x}_i) \exp \left\{ \frac{\|\bar{x}_i - \bar{y}_j\|_2^2}{\hat{\varepsilon}} \right\} \rho_{\hat{\varepsilon}}(\bar{y}_j) + \mathcal{O}_n^{(\varepsilon)} \left(\max \left\{ E\sqrt{\log p}, E^2\sqrt{p \log p} \right\} \right) \\
&= \int_{\mathcal{M}} \rho_{\hat{\varepsilon}}(\bar{x}_i) \mathcal{K}_{\hat{\varepsilon}}(\bar{x}_i, y) \rho_{\hat{\varepsilon}}(y) \omega(y) d\mu(y) + \mathcal{O}_n^{(\varepsilon)} \left(\sqrt{\frac{\log n}{n}} \right) + \mathcal{O}_n^{(\varepsilon)} \left(\max \left\{ E\sqrt{\log p}, E^2\sqrt{p \log p} \right\} \right) \\
&= 1 + \mathcal{O}_n^{(\varepsilon)} \left(\max \left\{ E\sqrt{\log p}, E^2\sqrt{p \log p}, \sqrt{\frac{\log m}{m}} \right\} \right), \tag{103}
\end{aligned}$$

for all $i \in [m]$, where we used the fact that $\sqrt{\log n/n} \leq 2\sqrt{\log m/m}$ for all sufficiently large m under Assumption 2, recalling also that $m \leq n$.

We are now in a position to apply Lemma 8 using the approximate scaling of \tilde{K} according to (102) and (103). We first evaluate and bound the different quantities appearing in Lemma 8. Recall that $r_i = \sqrt{n/m}$ and $c_j = \sqrt{m/n}$. Consequently, $s = \|\mathbf{r}\|_1 = \|\mathbf{c}\|_1 = \sqrt{mn}$ and

$$\bar{r}_i = \frac{r_i}{\sqrt{s}} = \frac{n^{1/4}}{m^{3/4}}, \quad \bar{c}_j = \frac{c_j}{\sqrt{s}} = \frac{m^{1/4}}{n^{3/4}}. \tag{104}$$

Hence, according to (100),

$$C_1 = \min_i \left\{ \frac{\hat{\alpha}_i}{\bar{r}_i} \right\} \geq C'_1(\varepsilon) \left(\frac{m}{n} \right)^{3/4}, \tag{105}$$

$$C_2 = \min_j \left\{ \frac{\hat{\beta}_j}{\bar{c}_j} \right\} \geq C'_2(\varepsilon) \left(\frac{n}{m} \right)^{3/4}, \tag{106}$$

for some constants $C'_1(\varepsilon), C'_2(\varepsilon) > 0$ (which may depend on ε), where we used the facts that ρ_{ε} is positive and continuous on a compact domain (and thus bounded from below away from zero) and that $\|\bar{x}_i\|_2, \|\bar{y}_j\|_2 \leq C$ by Assumption 1. Note that by (99) and Assumption 1,

$$C'_3(\varepsilon) \left[1 + \mathcal{O}_n^{(\varepsilon)} \left(\max \left\{ E\sqrt{\log p}, E^2\sqrt{p \log p} \right\} \right) \right] \leq \tilde{K}_{i,j} \leq C'_4(\varepsilon) \left[1 + \mathcal{O}_n^{(\varepsilon)} \left(\max \left\{ E\sqrt{\log p}, E^2\sqrt{p \log p} \right\} \right) \right], \tag{107}$$

for some constants $C'_3(\varepsilon), C'_4(\varepsilon) > 0$ for all sufficiently large n . Overall, applying Lemma 8 with $A = \tilde{K}$ and $(\hat{\alpha}, \hat{\beta})$ from (100), and after some manipulation, it can be verified that there exists a pair of positive vectors (α', β') that scales \tilde{K} to row sums \mathbf{r} and column sums \mathbf{c} , such that

$$\frac{|\alpha'_i - \hat{\alpha}_i|}{\hat{\alpha}_i} \leq \mathcal{O}_n^{(\varepsilon)} \left(\max \left\{ E\sqrt{\log p}, E^2\sqrt{p \log p}, \sqrt{\frac{\log m}{m}} \right\} \right), \tag{108}$$

$$\frac{|\beta'_j - \hat{\beta}_j|}{\hat{\beta}_j} \leq \mathcal{O}_n^{(\varepsilon)} \left(\max \left\{ E\sqrt{\log p}, E^2\sqrt{p \log p}, \sqrt{\frac{\log m}{m}} \right\} \right), \tag{109}$$

for all $i \in [m]$ and $j \in [n]$.

Finally, since $(\tilde{\alpha}, \tilde{\beta})$ from (94) is a pair of scaling factors of \tilde{K} , we can write

$$\begin{aligned}
W_{i,j} &= \alpha_i K_{i,j} \beta_j = \tilde{\alpha}_i \tilde{K}_{i,j} \tilde{\beta}_j = \alpha'_i \tilde{K}_{i,j} \beta'_j \\
&= \hat{\alpha}_i \tilde{K}_{i,j} \hat{\beta}_j \left[1 + \mathcal{O}_n^{(\varepsilon)} \left(\max \left\{ E\sqrt{\log p}, E^2\sqrt{p \log p}, \sqrt{\frac{\log m}{m}} \right\} \right) \right] \\
&= \frac{1}{(\pi \hat{\varepsilon})^{d/2} \sqrt{mn}} \rho_{\hat{\varepsilon}}(\bar{x}_i) \exp \left\{ -\frac{\|\bar{x}_i\|_2^2}{\hat{\varepsilon}} \right\} \exp \left\{ \frac{2\langle \bar{x}_i, \bar{y}_j \rangle}{\hat{\varepsilon}} \right\} \exp \left\{ -\frac{\|\bar{y}_j\|_2^2}{\hat{\varepsilon}} \right\} \rho_{\hat{\varepsilon}}(\bar{y}_j) \\
&\quad \times \left[1 + \mathcal{O}_n^{(\varepsilon)} \left(\max \left\{ E\sqrt{\log p}, E^2\sqrt{p \log p}, \sqrt{\frac{\log m}{m}} \right\} \right) \right], \tag{110}
\end{aligned}$$

for all $i \in [m]$ and $j \in [n]$, where we used (99) and (100) in the last transition. The proof of Theorem 4 follows immediately from the definitions of \mathcal{W}_ε and \mathcal{K}_ε in (25) and Assumption 1.

Appendix F Proof of Corollary 5

According to the definition of P in (13), we can write

$$\begin{aligned} & \left\| P[f]_{(\bar{x}, \bar{y})} - [\mathcal{P}_{\varepsilon/(a_1 a_2)} f]_{(\bar{x}, \bar{y})} \right\|_\infty \\ &= \max \left\{ \left\| \sqrt{\frac{m}{n}} W[h]_{\bar{y}} - [\mathcal{W}_{\varepsilon/(a_1 a_2)} h]_{\bar{x}} \right\|_\infty, \left\| \sqrt{\frac{n}{m}} W^T[g]_{\bar{y}} - [\mathcal{W}_{\varepsilon/(a_1 a_2)} g]_{\bar{x}} \right\|_\infty \right\}. \end{aligned} \quad (111)$$

Using Theorem 4, we have

$$\sqrt{\frac{m}{n}} W_{i, \cdot} [h]_{\bar{y}} = \frac{1}{n} \sum_{j=1}^n \mathcal{W}_{\varepsilon/(a_1 a_2)}(\bar{x}_i, \bar{y}_j) h(\bar{y}_j) + \mathcal{O}_n^{(\varepsilon)} \left(\max \left\{ E \sqrt{\log p}, E^2 \sqrt{p \log p}, \sqrt{\frac{\log m}{m}} \right\} \right), \quad (112)$$

where we used the fact that \mathcal{W}_ε and h are bounded over \mathcal{M} by universal constants according to Assumption 1 and the conditions in Corollary 5. Next, we apply Hoeffding's inequality to obtain

$$\begin{aligned} \sqrt{\frac{m}{n}} W_{i, \cdot} [h]_{\bar{y}} &= \int_{\mathcal{M}} \mathcal{W}_{\varepsilon/(a_1 a_2)}(\bar{x}_i, y) h(y) \omega(y) d\mu(y) \\ &\quad + \mathcal{O}_n^{(\varepsilon)} \left(\sqrt{\frac{\log n}{n}} \right) + \mathcal{O}_n^{(\varepsilon)} \left(\max \left\{ E \sqrt{\log p}, E^2 \sqrt{p \log p}, \sqrt{\frac{\log m}{m}} \right\} \right) \\ &= \{\mathcal{W}_{\varepsilon/(a_1 a_2)} h\}(\bar{x}_i) + \mathcal{O}_n^{(\varepsilon)} \left(\max \left\{ E \sqrt{\log p}, E^2 \sqrt{p \log p}, \sqrt{\frac{\log m}{m}} \right\} \right), \end{aligned} \quad (113)$$

for any $i \in [m]$ according to Assumption 2. Using the union bound, we have

$$\left\| \sqrt{\frac{m}{n}} W[h]_{\bar{y}} - [\mathcal{W}_{\varepsilon/(a_1 a_2)} h]_{\bar{x}} \right\|_\infty = \mathcal{O}_n^{(\varepsilon)} \left(\max \left\{ E \sqrt{\log p}, E^2 \sqrt{p \log p}, \sqrt{\frac{\log m}{m}} \right\} \right). \quad (114)$$

By an analogous derivation, it can be verified that

$$\left\| \sqrt{\frac{n}{m}} W^T[g]_{\bar{y}} - [\mathcal{W}_{\varepsilon/(a_1 a_2)} g]_{\bar{x}} \right\|_\infty = \mathcal{O}_n^{(\varepsilon)} \left(\max \left\{ E \sqrt{\log p}, E^2 \sqrt{p \log p}, \sqrt{\frac{\log m}{m}} \right\} \right). \quad (115)$$

Overall, we obtain

$$\left\| P[f]_{(\bar{x}, \bar{y})} - [\mathcal{P}_{\varepsilon/(a_1 a_2)} f]_{(\bar{x}, \bar{y})} \right\|_\infty = \mathcal{O}_n^{(\varepsilon)} \left(\max \left\{ E \sqrt{\log p}, E^2 \sqrt{p \log p}, \sqrt{\frac{\log m}{m}} \right\} \right). \quad (116)$$

Let us define $f_1 = \mathcal{P}_{\varepsilon/(a_1 a_2)} f$. Clearly, $f_1 \in \mathcal{H}$ and is bounded on \mathcal{M} , hence (116) also holds when replacing f with f_1 . We now have

$$\begin{aligned} & \left\| P^2[f]_{(\bar{x}, \bar{y})} - [\mathcal{P}_{\varepsilon/(a_1 a_2)}^2 f]_{(\bar{x}, \bar{y})} \right\|_\infty = \left\| P^2[f]_{(\bar{x}, \bar{y})} - [\mathcal{P}_{\varepsilon/(a_1 a_2)} f_1]_{(\bar{x}, \bar{y})} \right\|_\infty \\ & \leq \left\| P^2[f]_{(\bar{x}, \bar{y})} - P[f_1]_{(\bar{x}, \bar{y})} \right\|_\infty + \left\| P[f_1]_{(\bar{x}, \bar{y})} - [\mathcal{P}_{\varepsilon/(a_1 a_2)} f_1]_{(\bar{x}, \bar{y})} \right\|_\infty \\ & \leq \max_i \left\{ \sum_j P_{i,j} \right\} \left\| P[f]_{(\bar{x}, \bar{y})} - [f_1]_{(\bar{x}, \bar{y})} \right\|_\infty + \mathcal{O}_n^{(\varepsilon)} \left(\max \left\{ E \sqrt{\log p}, E^2 \sqrt{p \log p}, \sqrt{\frac{\log m}{m}} \right\} \right) \\ & \leq \mathcal{O}_n^{(\varepsilon)} \left(\max \left\{ E \sqrt{\log p}, E^2 \sqrt{p \log p}, \sqrt{\frac{\log m}{m}} \right\} \right), \end{aligned} \quad (117)$$

where we used (116) and the fact that P is row-stochastic ($\sum_j P_{i,j} = 1$ for all i) in the last transition. We can proceed recursively by defining $f_k = \mathcal{P}_{\varepsilon/(a_1 a_2)} f_{k-1}$ for $k = 2, \dots, t$, repeating the process in (116) and (117) for each step. Eventually, we obtain

$$\left\| P^t [f]_{(\bar{x}, \bar{y})} - \left[\mathcal{P}_{\varepsilon/(a_1 a_2)}^t f \right]_{(\bar{x}, \bar{y})} \right\|_{\infty} = \mathcal{O}_n^{(\varepsilon)} \left(\max \left\{ E\sqrt{\log p}, E^2\sqrt{p \log p}, \sqrt{\frac{\log m}{m}} \right\} \right). \quad (118)$$

The proof of Corollary 5 follows immediately from the fact that $\max \left\{ E\sqrt{\log p}, E^2\sqrt{p \log p}, \sqrt{\frac{\log m}{m}} \right\} \rightarrow 0$ as $n \rightarrow \infty$ by Assumptions 1 and 2.

Appendix G Proof of Corollary 6

According to Theorem 4, we have

$$\begin{aligned} \frac{\sqrt{mn}W_{i,j}}{\hat{\mathcal{W}}_{\hat{\varepsilon}}(\bar{x}_i, \bar{y}_j)} &= \frac{\rho_{\hat{\varepsilon}}(\bar{x}_i)\mathcal{K}_{\hat{\varepsilon}}(\bar{x}_i, \bar{y}_j)\rho_{\hat{\varepsilon}}(\bar{y}_j) + \mathcal{O}_n^{(\varepsilon)} \left(\max \left\{ E\sqrt{\log p}, E^2\sqrt{p \log p}, \sqrt{\frac{\log m}{m}} \right\} \right)}{\frac{\mathcal{K}_{\hat{\varepsilon}}(\bar{x}_i, \bar{y}_j)}{\sqrt{\omega(\bar{x}_i)\omega(\bar{y}_j)}}} \\ &= \rho_{\hat{\varepsilon}}(\bar{x}_i)\rho_{\hat{\varepsilon}}(\bar{y}_j)\sqrt{\omega(\bar{x}_i)\omega(\bar{y}_j)} + \mathcal{O}_n^{(\varepsilon)} \left(\max \left\{ E\sqrt{\log p}, E^2\sqrt{p \log p}, \sqrt{\frac{\log m}{m}} \right\} \right), \end{aligned} \quad (119)$$

for all $i \in [m]$ and $j \in [n]$, where $\hat{\varepsilon}$ is from (100) and we used the properties of Definition 10, the fact that $\mathcal{K}_{\hat{\varepsilon}}(\bar{x}_i, \bar{y}_j) \geq \exp\{-4C^2/\hat{\varepsilon}\} \geq \exp\{-4C^4/\varepsilon\}$ by Assumption 1, and the fact that $\omega(x)$ is continuous on \mathcal{M} and thus upper bounded by a global constant. Applying Hoeffding's inequality, we can write

$$\begin{aligned} \frac{1}{mn} \sum_{i,j} \left| \frac{\sqrt{mn}W_{i,j}}{\hat{\mathcal{W}}_{\hat{\varepsilon}}(\bar{x}_i, \bar{y}_j)} - 1 \right| &= \int_{\mathcal{M}} \int_{\mathcal{M}} \left| \rho_{\hat{\varepsilon}}(x)\rho_{\hat{\varepsilon}}(y)\sqrt{\omega(x)\omega(y)} - 1 \right| \omega(x)\omega(y) d\mu(x)d\mu(y) \\ &\quad + \mathcal{O}_n^{(\varepsilon)} \left(\max \left\{ E\sqrt{\log p}, E^2\sqrt{p \log p}, \sqrt{\frac{\log m}{m}} \right\} \right). \end{aligned} \quad (120)$$

According to Theorem 2.6 in [33], we have

$$\rho_{\varepsilon}(x) = \frac{1}{\sqrt{\omega(x)}} + e_{\varepsilon}(x), \quad \int_{\mathcal{M}} |e_{\varepsilon}(x)| d\mu(x) \leq c_1\varepsilon, \quad (121)$$

for all $\varepsilon \leq \varepsilon_0$, where $c_1, \varepsilon_0 > 0$ are some global constants. We thus obtain

$$\begin{aligned} \frac{1}{mn} \sum_{i,j} \left| \frac{\sqrt{mn}W_{i,j}}{\hat{\mathcal{W}}_{\hat{\varepsilon}}(\bar{x}_i, \bar{y}_j)} - 1 \right| &= \int_{\mathcal{M}} \int_{\mathcal{M}} \left| \frac{e_{\varepsilon}(x)}{\sqrt{\omega(y)}} + \frac{e_{\varepsilon}(y)}{\sqrt{\omega(x)}} + e_{\varepsilon}(x)e_{\varepsilon}(y) \right| \omega(x)\omega(y) d\mu(x)d\mu(y) \\ &\quad + \mathcal{O}_n^{(\varepsilon)} \left(\max \left\{ E\sqrt{\log p}, E^2\sqrt{p \log p}, \sqrt{\frac{\log m}{m}} \right\} \right) \\ &\leq 2 \left(\int_{\mathcal{M}} |e_{\varepsilon}(x)| \omega(x) d\mu(x) \right) \left(\int_{\mathcal{M}} \sqrt{\omega(x)} d\mu(x) \right) + \left(\int_{\mathcal{M}} |e_{\varepsilon}(x)| \omega(x) d\mu(x) \right)^2 \\ &\quad + \mathcal{O}_n^{(\varepsilon)} \left(\max \left\{ E\sqrt{\log p}, E^2\sqrt{p \log p}, \sqrt{\frac{\log m}{m}} \right\} \right) \\ &\leq c_2\varepsilon + c_3\varepsilon^2 + \mathcal{O}_n^{(\varepsilon)} \left(\max \left\{ E\sqrt{\log p}, E^2\sqrt{p \log p}, \sqrt{\frac{\log m}{m}} \right\} \right), \end{aligned} \quad (122)$$

for some global constants $c_2, c_3 > 0$ that may depend on \mathcal{M} and ω (which is bounded on \mathcal{M}). Since $c_3\varepsilon^2$ is smaller than $c_2\varepsilon$ for all sufficiently small ε , the proof is concluded.

Appendix H Supplementary Notes on Numerical Results

Additional alignment evaluations. For each of the simulation experiments, we also consider an alternative metric to evaluate the performance of each method in aligning the shared manifold structures (i.e., torus, or clusters) between the two datasets (batches). Specifically, once the joint embeddings are obtained, we calculate the Davies-Bouldin (D-B) index with respect to the dataset/batch labels. For a given integrated dataset consisting of K batches C_1, C_2, \dots, C_K , the D-B index is defined as

$$\text{D-B index} = \frac{1}{K} \sum_{k=1}^K \max_{j \neq k} \frac{S_k + S_j}{M_{kj}}, \quad (123)$$

where

$$S_i = \left[\frac{1}{|C_k|} \sum_{i \in C_k} \|X_i - A_k\|_2^2 \right]^{-1/2}, \quad M_{kj} = \|A_k - A_j\|_2, \quad (124)$$

with A_k being the centroid of batch k of size $|C_k|$, X_i is the embedding of i -th data point. A higher D-B index indicates stronger mixing or a better alignment of the batches.

For the alignment of single-cell omics samples, we use the Silhouette index with respect to the cell type annotations to evaluate the quality of the joint embeddings. For each embedded dataset containing n points, for each data point i , we define the Silhouette index

$$s(i) = \begin{cases} 1 - a(i)/b(i) & \text{if } a(i) < b(i) \\ 0 & \text{if } a(i) = b(i) \\ b(i)/a(i) - 1 & \text{if } a(i) > b(i) \end{cases}, \quad (125)$$

where $a(i)$ is the mean distance between i and all other data points in the same cluster, and $b(i)$ is the smallest mean distance of i to all points in any other cluster (i.e., in any cluster of which i is not a member). For each embedding, we report the mean Silhouette index $\bar{s} = n^{-1} \sum_{i=1}^n s(i)$ across all the data points.

Hyperparameters. The proposed EOT eigenmap requires specifying three major hyperparameters: the kernel bandwidth or entropy regularization parameter $\epsilon > 0$, the diffusion steps $t \geq 0$, and the embedding dimension q . In practice, these parameters are user-specified depending on the specific applications, whose determination should be subject to critical procedures described in community guidelines [69, 70] to enhance contextual fitness, stability, and reproducibility.

Below we provide some general recommendations which may be considered as a default setting for exploratory analysis. Specifically, the bandwidth parameter ϵ can be determined as the median of pairwise squared distances between the datasets, that is, the median of $\{\|x_i - y_j\|_2^2\}_{1 \leq i \leq m, 1 \leq j \leq n}$. This procedure has been found robust against high-dimensional noise and theoretically appealing [19, 20]. We followed such a recommendation throughout our simulations and real data analysis, demonstrating its practical efficacy. The embedding dimension q depends on the informativeness of the leading singular values and vectors of the EOT plan W . Here we recommend setting $q = \max_{1 \leq i \leq m-1} \{i : s_i/s_{i+1} \geq 1 + \mathbf{s}\}$, where $\mathbf{s} = 0.02$. For the diffusion parameter $t \geq 0$, based on our discussion after Proposition 3, we recommend setting $t = 0$ if one is more confident about the embedding dimension q , and setting $t > 0$ otherwise.

Implementation details. For the joint embedding method ‘‘seurat’’ evaluated in our experiments, we consider its core step described in the original publication [60], where the low-dimensional embeddings for datasets $X \in \mathbb{R}^{m \times p}$ and $Y \in \mathbb{R}^{n \times p}$ are defined as the leading left and right singular vectors of the product matrix XY^\top . For standard kernel methods such as ‘‘kpca’’ and ‘‘j-kpca’’, we again follow [19] and use the median of the respective pairwise distances as the kernel bandwidth.

To pre-process the single-cell gene expression data, we performed quality control, normalization, and scaling of the raw count data using the R functions `CreateSeuratObject`, `NormalizeData` and `ScaleData` under default settings as incorporated in the R package `Seurat`. We also applied the R function `FindVariableFeatures` in `Seurat` to identify $p = 1000$ (three sample alignment tasks) or $p = 2000$ (SCORCH

multiomics analysis) most variable genes for subsequent analysis. For the the single-cell chromatin accessibility data, we used R functions `RunTFIDF` and `FindTopFeatures` from the R package `Signac` to normalize the count matrix and find the $p = 5000$ most variable accessible chromatin regions.

In our analysis of the SCORCH multiomics dataset, we selected the embedding dimension q based on the following eigenvalue thresholding method. Suppose $\{s_i\}_{i=1}^m$ be the singular values of W . Then we choose $q = \max_{1 \leq i \leq m-1} \{i : s_i/s_{i+1} \geq 1 + s\}$, where $s = 0.02$.

Appendix I Supplementary Figures

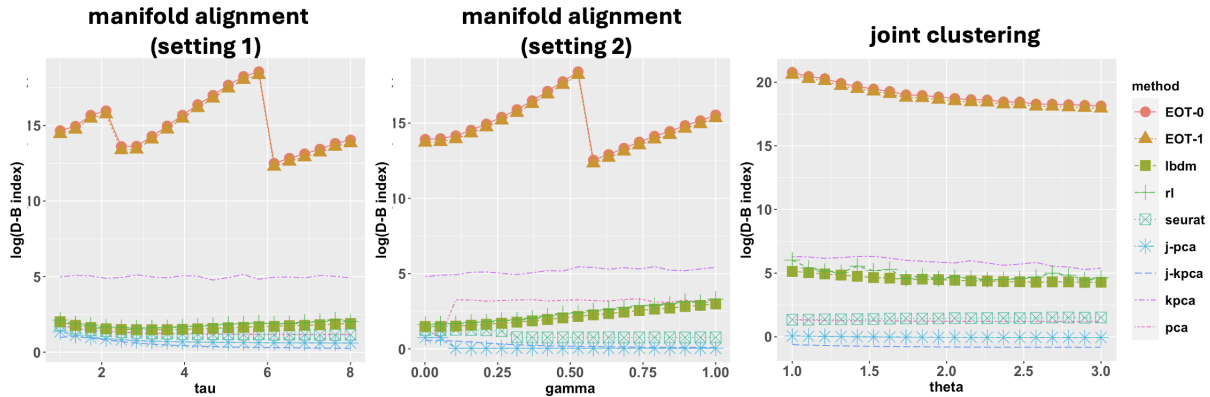


Figure S1: Comparison of Davies-Bouldin index of nine integration methods in various simulations. Left and Middle: simulations for noisy manifold alignment, setting 1 (left) and setting 2 (middle). Right: simulations for joint clustering. Our results indicate superior performance of the proposed methods (“EOT-0” and “EOT-1”) in aligning the latent structures.

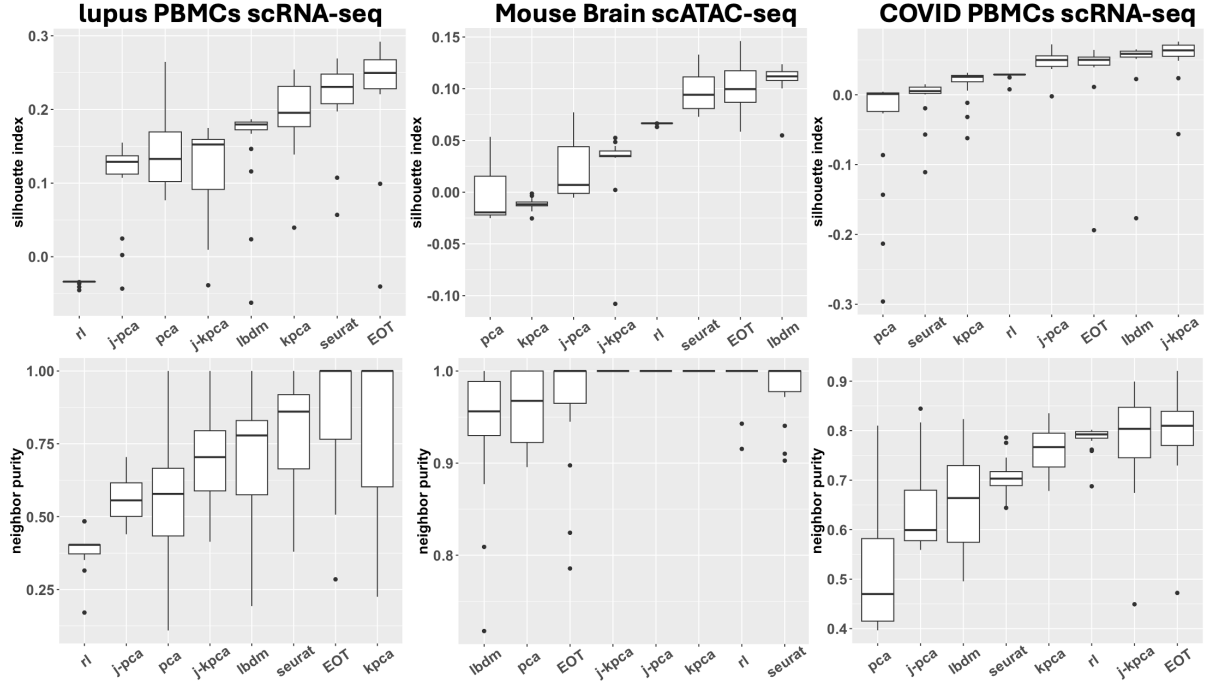


Figure S2: Comparison of mean Silhouette index (Top row) and neighbor purity score (Bottom row) of eight integration methods in three pairs of single-cell omics data, where each boxplot contains the metrics for each method across a range of embedding dimensions q (from 2 to 20). Left: scRNA-seq data of human PBMCs under different experimental conditions. Middle: scATAC-seq data of mouse brain cells from different studies. Right: scRNA-seq data of human PBMCs from different samples. Our results indicate the advantages of the proposed method (“EOT”) in identifying and aligning the different cell types across datasets, and its robustness with respect to the choice of embedding dimension q .

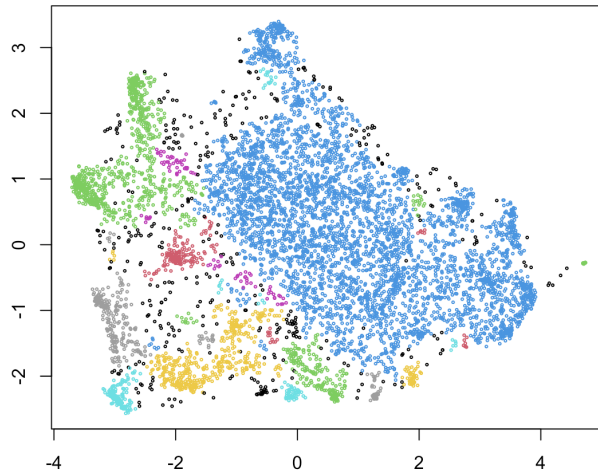


Figure S3: Joint clustering of genes and accessible chromatin regions identified by DBSCAN algorithm [24]. Each cluster of features has a distinct color, whereas the black dots correspond to the “singletons” identified by DBSCAN.